catalysts

MDPI

*Article*

# Photocatalytic Efficacy of Heterocyclic Base Grafted Chitosan Magnetite Nanoparticles on Sorption of Pb(II); Application on Mining Effluent

**Mohammed F. Hamza [1,2,*], Adel E.-S. Goda [3], Shunyan Ning [2], Hamed I. Mira [2], Adel A.-H. Abdel-Rahman [4], Yuezhou Wei [1,5,*], Toyohisa Fujita [6,7], Hamada H. Amer [8], Saad H. Alotaibi [8] and Amr Fouda [9]**

1 School of Nuclear Science and Technology, University of South China, Hengyang 421001, China
2 Nuclear Materials Authority, POB 530, El-Maadi, Cairo 11728, Egypt; ningshunyan@usc.edu.cn (S.N.); hamedmira@yahoo.com (H.I.M.)
3 Tanta Higher Institute of Engineering and Technology, Tanta 31739, Egypt; adelgoda1969@gmail.com
4 Chemistry Department, Faculty of Science, Menofia University, Shebin El-Kom 32511, Egypt; adelnassar63@yahoo.com
5 School of Nuclear Science and Engineering, Shanghai Jiao Tong University, Shanghai 200240, China
6 School of Resources, Environment and Materials, Guangxi University, Nanning 530004, China; fujitatoyohisa@gxu.edu.cn
7 School of Chemistry and Chemical Engineering, Guangxi University, Nanning 530004, China
8 Department of Chemistry, Turabah University College, Taif University, Taif 21944, Saudi Arabia; h.amer@tu.edu.sa (H.H.A.); s.alosaimi@tu.edu.sa (S.H.A.)
9 Botany and Microbiology Department, Faculty of Science, Al-Azhar University, Cairo 11884, Egypt; amr_fh83@azhar.edu.eg
* Correspondence: m_fouda21@hotmail.com (M.F.H.); yzwei@sjtu.edu.cn (Y.W.); Tel.: +20-111-668-1228 (M.F.H.); +86-771-322-4990 (Y.W.)

check for updates

**Citation:** Hamza, M.F.; Goda, A.E.-S.; Ning, S.; Mira, H.I.; Abdel-Rahman, A.A.-H.; Wei, Y.; Fujita, T.; Amer, H.H.; Alotaibi, S.H.; Fouda, A. Photocatalytic Efficacy of Heterocyclic Base Grafted Chitosan Magnetite Nanoparticles on Sorption of Pb(II); Application on Mining Effluent. *Catalysts* **2022**, *12*, 330. https://doi.org/10.3390/catal12030330

Academic Editor: María Victoria López Ramón

Received: 18 February 2022
Accepted: 9 March 2022
Published: 14 March 2022



**Abstract:** Development of bio-based sorbents (i.e., chitosan moieties) at nanoscale size for the removal of metal contaminants is the main target of this research. Grafting with thiazole heterocyclic derivative gives fast kinetics sorption, highly metal loading, and good recyclability for mining leaching solution. Different analyses tools including (thermogravimetric analysis (TGA), scanning electron microscope and energy dispersive spectroscopy (SEM-EDX), X-ray diffraction (XRD), Fourier transform infrared (FTIR), BET surface area (nitrogen sorption desorption), titration, and TEM (transmission electron microscopy)) were used to investigate the chemical and textural properties of the functionalized sorbent. The sorption was measured in normal visible light and under UV emission. The highest capacity was measured at pH 5, which reached 0.251 mmol Pb $g^{-1}$ in visible light compared with 0.346 mmol Pb $g^{-1}$ under UV for the pristine crosslinked chitosan (MCc). The sorption performances were improved by functionalization; (0.7814 and 1.014 mmol Pb $g^{-1}$) for the functionalized sorbent (MCa-ATA) under visible light and UV, respectively. PFORE (pseudo-first-order rate equation) and RIDE (resistance to intraparticle diffusion) fit kinetics, the Sips equation is the most fit profile for the sorption isotherms for the MCc in either light and UV processes, while PFORE and RIDE for kinetics under light and UV for MCa-ATA and Sips in light and Sips and Langmuir under the UV emission. Finally, the sorbent was investigated toward a raffinate solution from ore processing and shows promising extraction tools for the most interesting elements.

**Keywords:** photocatalysis; bio-based materials; metal-contamination; nanoscale particles

## 1. Introduction

Water contamination is one of the significant problems facing most developing countries. The contamination sources are varied; most of them are derived from industrial activities, agricultural discharges, population growth, and vast urbanizations [1,2]. Accumulation of toxic and hazardous metals in the food chain, as well as their dramatic effects

on human beings clearly explains the drastic need for controlling the contamination of water and controlling the industries for limitation of their impacts on the surrounding environment and water bodies [3,4].

Contaminated effluents contain highly toxic compounds such as residual dyes, chemicals, heavy metals, salts, surfactants, and chlorinated substances that must be refined before reuse [5] or in-plant irrigation [6]. The chemical treatment, physical methods (i.e., ozonation, oxidations, adsorption, filtration, reverse osmosis, froth flotations, electrocoagulation, and flocculation), or biological methods are extensively used for treatment processes, but the main problems that face most of these methods are insufficient removal and the cost-ineffectiveness [7]. These methods also require more time, non-biodegradable substances, and the reverse effects of the toxic substances on the microorganisms, where biological treatment is used [1,8].

Biopolymers and biosorbents have been used as efficient sorbents for heavy and economically valued metal recovery [9–11]. The presence of polarized groups in the biopolymers makes a profit for grafting and modification; among these groups are amine and hydroxyl (in chitosan, [12]) or carboxylic groups (in alginate, [13,14]). These composites have been used as encapsulating materials (through hydrogel formation [15–17]) and/or for functionalization [18,19]. The presences of these functional groups (hydroxyl, carboxyl, and amine groups) support a further reactivity for further chemical grafting.

Nanoparticles have attracted attention due to their fast kinetics and safe, unique properties [20]. Recently, nanoparticles have been used in various fields such as medicine, agriculture, the textile industry, pharmaceuticals, cosmetics, photocatalytic, and archeological manuscript preservation [21–26]. The nanoparticles were synthesized by several procedures (physical, chemical, and biological methods) [27,28]. The use of the biological route for NPs synthesis is a preferential method over others [29], due to its environmentally friendly, easily scale-up, biocompatibility, and inexpensive process. The most familiar NPs that are generated by this method include ZnO, Ag, Cu, Au, CuO, MgO, $Fe_2O_3$, and Se [30,31].

Several processes can be used for the recovery of heavy metals, such as solvent extraction [32–34], precipitation [35] (which are usually used for high-grade metal concentration [36]), bioreduction [37], and electrochemical reduction [38]. Iron-core (magnetic nano- or microparticles) [18,27,39] sorbents facilitate the sorption ability as well as facilitate the solid/liquid separation of the composite material. This magnetite core incorporation into biopolymer [40] and also polymers [41] allows separation of the sorbent at the end step of sorption, while reducing the particle size, minimizing the mass transfer properties [42–47], and improving the biological activities (i.e., imidazole and thiazole-based ligands), as well as improving the selectivity and sorption capacity. Dhivya et al. [48] investigated the inhibitory effects of the chitosan/magnetite NPs and magnetite NPs against *Escherichia coli* KL226. On the other hand, Hamza et al., [49,50] studied the effect of different doses of functionalized chitosan nano and microparticles on various strains of Gram-positive, Gram-negative bacteria, and unicellular fungi, and also detect the MIC (minimum inhibition concentration) values. Moreover, various biosynthesized NPs have been used as a biocatalyst in the sorption of Cr ions from wastewater (real textile and tannery effluents), dye removal, and heavy metal extraction [24,51].

The main hypothesis of the current study is the synthesis of functionalized chitosan to investigate their efficacy in the sorption of Pb and other heavy metals in real contaminated effluents under visible light and UV-emission. To accomplish this hypothesis, nano magnetite chitosan particles were synthesized and functionalized with thiazole carboxylic acid derivative. Full physical and chemical characterization of synthesized bio-based sorbents were achieved by FT-IR (Fourier transform infrared) spectroscopy, XRD (X-ray diffraction), TEM (transmission electron microscopy), SEM-EDX (scanning electron microscope and energy dispersive spectroscopy), and TGA (thermogravimetric analysis). Moreover, the synthesized sorbent was used for the sorption of Pb(II) from synthetic solution and other heavy metals from real contaminated effluents in the mining area through pH, uptake

kinetics, and sorption isotherms, followed by studying the sorption from synthetic simulated nature solution under visible lights (L) and under UV emission to investigate the photocatalytic properties.

## 2. Results and Discussion

### *2.1. Sorbent Characterization*

#### 2.1.1. Textural Properties—BET, TEM, XRD, and SEM-EDX

The TEM analysis (Figure 1A) of the sorbent was indicated as a thin layer of organic particles over the magnetite NPs (dark spherical points); this was emphasized by the speed sorption performances and the limitation of intraparticle diffusion. The average size of the modified sorbent composite was closed to 10 μm (±2 μm), as shown from the SEM analysis of the sorbent in Figure 1B. It is characterized by a folded and irregular surface. From this Figure, it was shown that a randomness distribution of the magnetite throughout the polymer, also the agglomeration of the magnetite particles (dark black points). The type of dryness controls the physical properties that air-dry condition contributes to the shrinking of the hydrogel, while the freeze-drying or the $CO_2$ drying conditions save on the polymer network [52,53].

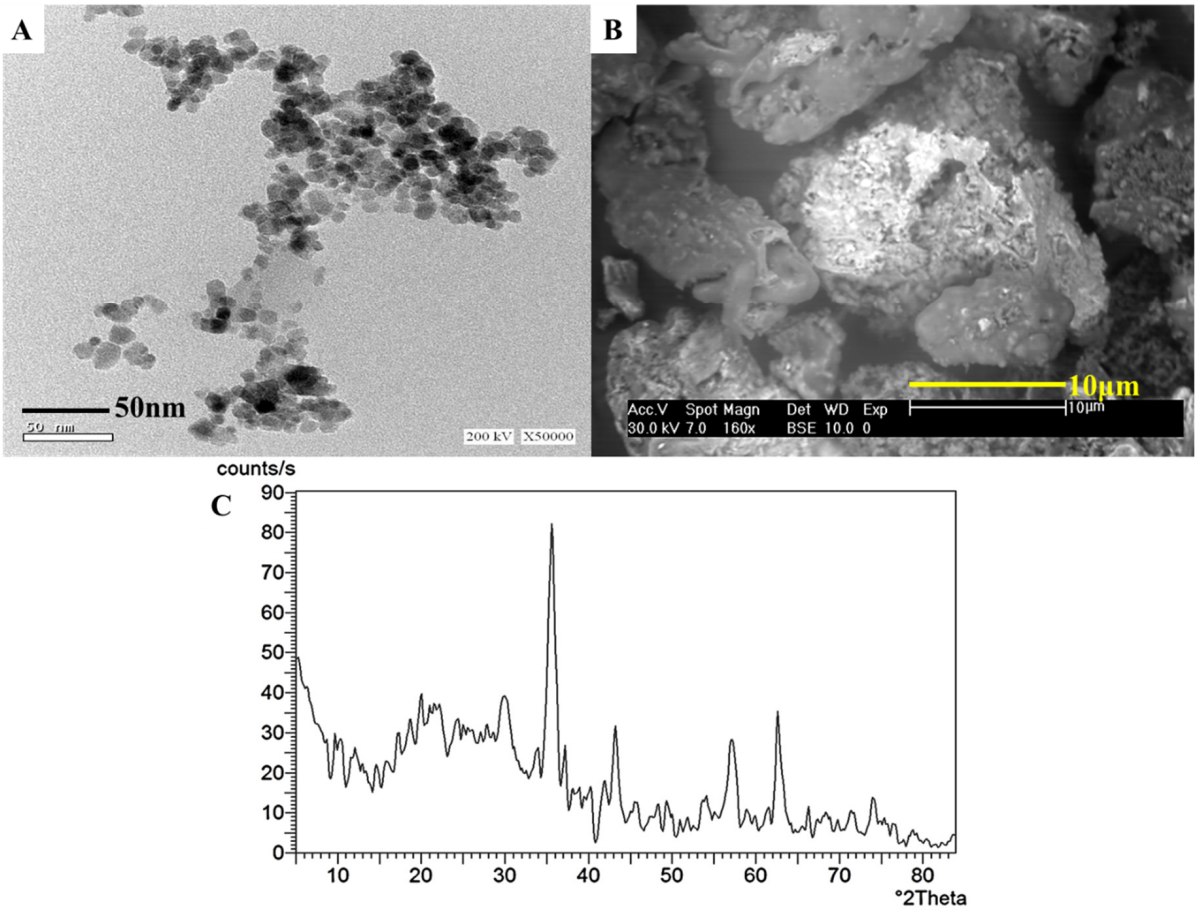


**Figure 1.** Transmission electron microscopy (TEM) (**A**), scanning electron microscope (SEM) (**B**), and X-ray diffraction (XRD) (**C**) analysis of the MCa-ATA sorbent.

The $N_2$ sorption/desorption isotherms were investigated by the BET surface area technique. This analysis confirms a poorly porous surface with a high specific surface area that ranged to 89.3 $m^2$ $g^{-1}$ for MCa-ATA. The porous volume was determined using the BJH method, which ranged about 15.7 $cm^3$ STP $g^{-1}$ of this sorbent, while MCc sorbent was recorded as 68.74 $m^2$ $g^{-1}$ and 13.99 $cm^3$ STP $g^{-1}$, respectively.

Figure 1C represents the XRD diffraction pattern analysis of the MCa-ATA sorbent. The magnetite was characterized by matching of nine peaks reported at 2θ = 18.2700, 30.2500, 35.5474, 37.3469, 43.1967, 57.0873, 62.6265, 81.4031, and 82.2235 degrees. These peak signals corresponded to the magnetite (JCPDS: 01-077-1545). Table S1 shows the diffraction patterns positions of the XRD peaks comparing to the reference file data. EDX analysis emphasized the modification through the different stages of synthesis. The appearance of the Cl ions (4.92%) in the sorbent surface verified the crosslinking and spacer arm modification, whereas decreasing this percent to 0.16% verified the replacement reaction with thiazole moiety. On the other hand, increasing the N percent from 4.17 to 7.89% as well as the creation of S (with a percent of 4.17%) gives an indication of the successful grafting of the heterocyclic moiety, as shown in Figure 2.

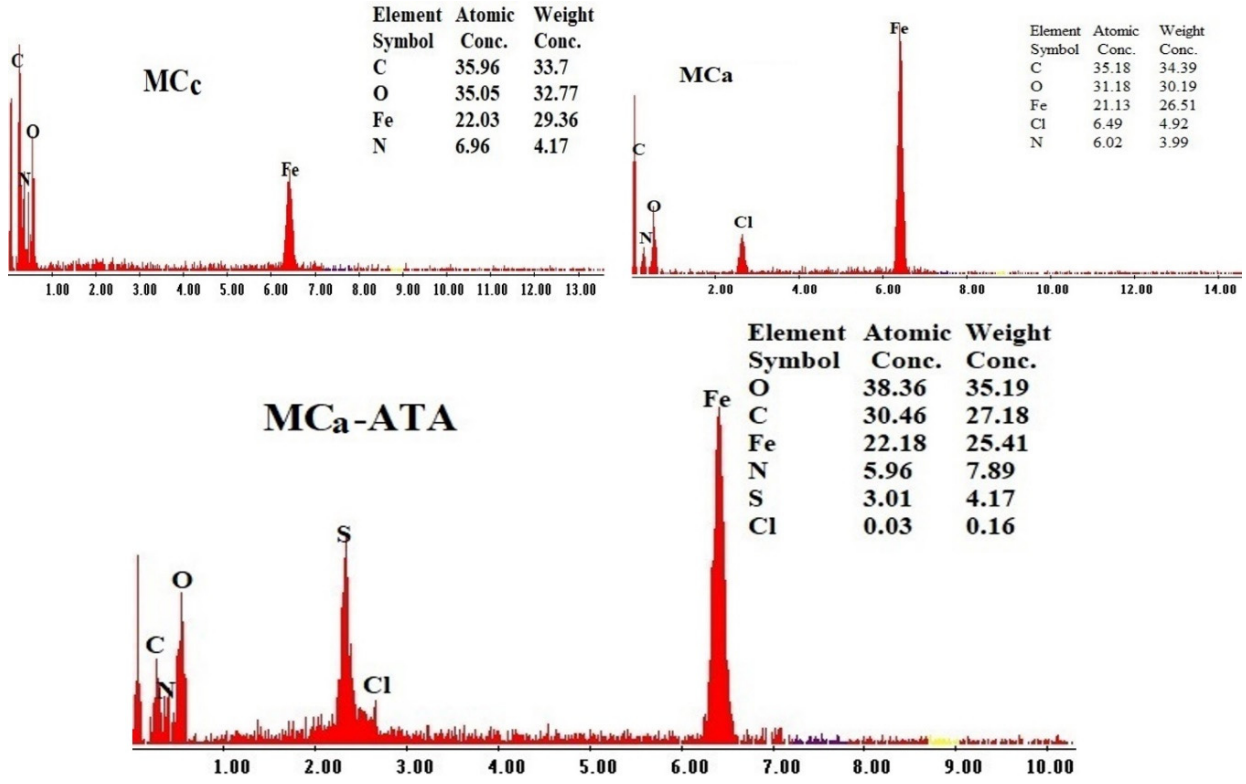


**Figure 2.** EDX data of the sorbent and after modification (MCc, Mca, and MCa-ATA).

### 2.1.2. TGA Analysis

The thermal degradation of sorbents was performed under a nitrogen atmosphere; Figure S1 shows the data of TGA and DrTG curves for MCc and MCa-ATA. Three steps were detected from the degradation profiles; the first stage for water release, which was assigned at 235.2 °C and 233.1 °C for MCc and MCa-ATA, respectively, with an average loss of about 9.89 and 8.848%. The second loss was limited for MCc than for functionalized sorbent, which performed at 279.2 °C for MCc with a loss of 19.1% and to 463.9 °C for MCa-ATA with a loss of 34.508%. This loss is related to the depolymerization of the chitosan backbone and the crosslinking bonds of amides. The last step in the thermal degradation was owed to the pyrolysis to char formation [54]. The weight loss of both polymers was 17.877 and 30.21% for MCc and MCa-ATA, respectively. This data was identical to those obtained by Gad [55], who found that the stability of copolymer is much more than homo one (pure components). The total loss from the pyrolysis is close to 46.9 and 73.566% for MCc and MCa-ATA, respectively.

2.1.3. FTIR Spectroscopy

The FTIR spectra are shown in Figure 3 for the sorbents (MCc and MCa-ATA), after Pb(II) sorption, and after the five sorption and desorption cycles. The broadness peaks at 3427, 3447, 3425, and 3412 $cm^{-1}$ for MCc, MCa-ATA, MCa-ATA+Pb, and after five cycles of sorption desorption, respectively, were related to OH and NH stretching bands, while those at 3197 $cm^{-1}$ and 3185 $cm^{-1}$ for MCa-ATA before and after desorption, respectively, was related to C-H of polysaccharide stretching bands. The peaks in the range of 2800 to 2900 $cm^{-1}$ were correlated to C-H vibration stretching. The C=O of the chitosan and the high intensity of this peak relate to the C=O, and C=C in the heterocyclic grafted moieties that are overlapped at 1638 and 1620 $cm^{-1}$, respectively. The intensity of this peak becomes decreased as Pb(II) sorption is performed, which appeared at 1621 $cm^{-1}$, then was restored as the desorption process was performed at 1610 $cm^{-1}$ with increasing intensity. The NH bending vibration was confirmed at 1513 $cm^{-1}$ for MCa-ATA and disappeared for loaded sorbent, then returned to appear at 1511 $cm^{-1}$ after desorption; this confirms the participation of the NH groups in the sorption mechanism. Other peaks are listed in Table 1 for MCc, MCa-ATA, after sorption, and after five cycles, which emphasize the successive modification and effective sorption as well as stability of the sorbent after desorption cycles by restoring the peaks.

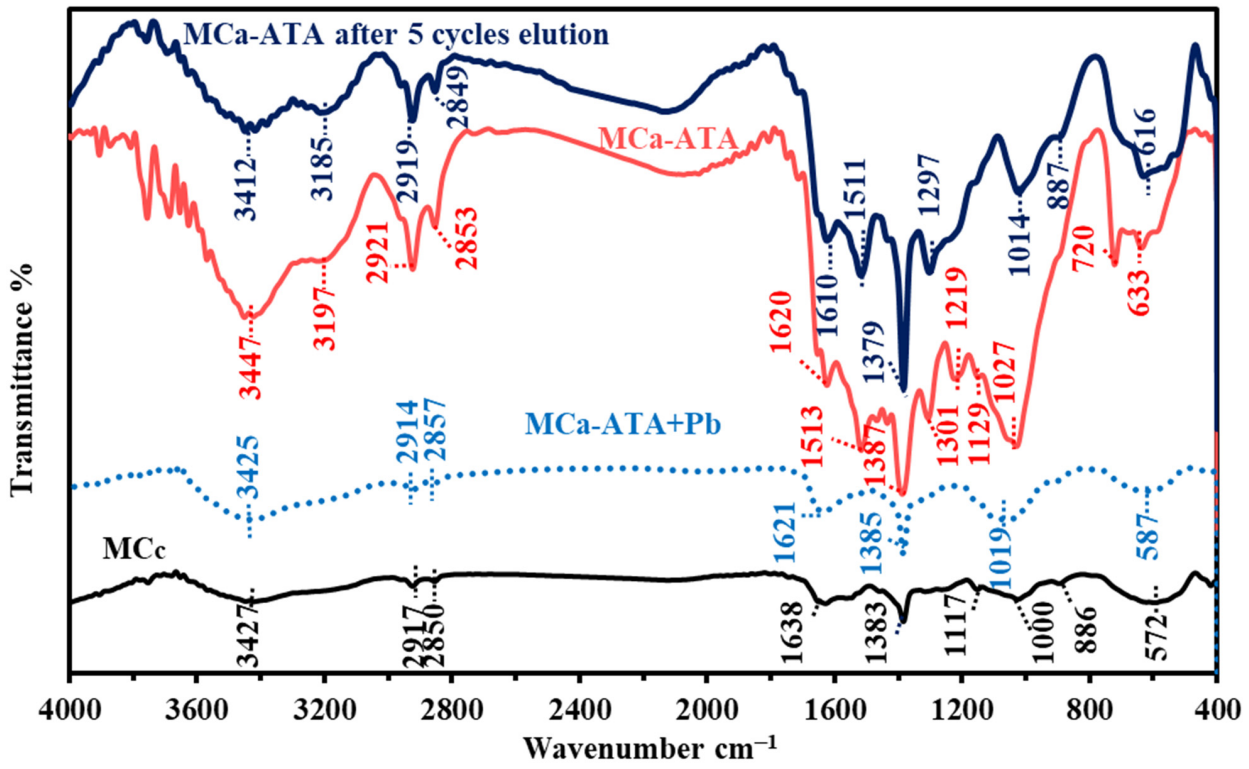


**Figure 3.** FTIR spectra of the MCc and MCa-ATA after sorption and after five cycles of sorption desorption.

2.1.4. Elemental Analysis

Table S2 reports the elemental analysis components of the MCc and MCa-ATA; the appearance of the sulfur element as grafting occurred of thiazole moieties on chitosan, confirmed the successive and effective grafting. It is noteworthy that as grafting was performed, the N content was increased from 3.51 mmol N $g^{-1}$ for MCc to 4.63 mmol N $g^{-1}$ for MCa-ATA, while little increase in the O contents was noticed (i.e., from 20.114 mmol O $g^{-1}$ to 20.65 mmol O $g^{-1}$, respectively), this is the other evidence for successive grafting of thiazole moieties. The EDX analysis (see Figure 2) indicates the perfect modifications through the appearance of Cl and S in the spacer arm and for the heterocyclic moieties grafting, respectively.

**Table 1.** Assignments of FTIR peaks for MCc and MCa-ATA before and after sorption and after five cycles of sorption desorption for Pb(II).

| Assignment | MCc | MCa-ATA | Loaded | Elution 5 Cycles | Ref. |
|---|---|---|---|---|---|
| O-H overlapped with N-H str. | 3427 | 3447, 3197 | 33,425 | 3412, 3185 | [56–58] |
| C-H str. | 2917, 2850 | 2921, 2853 | 2914, 2857 | 2919, 2849 | [59] |
| C=O str. | 1638 | 1620 | 1621 | 1610 | [57,60,61] |
| N-H bend. | | 1513 | | 1511 | [62] |
| $CH_3$ symm. def., C-N str. | 1383 | 1387, 1301 | 1385 | | [57,60,63] |
| C-O-C asymm. str., C-O str, and C-N str. | 1117 | 1219, 1129 | | 1297 | [56,61,64] |
| CO str. | 1000 | 1027 | | 1014 | [56] |
| Skeletal C-O str. | | | 1019 | | [56,57] |
| C-O- epoxy | 886 | | | 887 | [60] |
| C-O-S str. | | 720 | | | [64] |
| $-(CH_2)_n$ rocking and O-H out of plane bend., and/or C-S | 572 | 633 (broad) | 587 (broad) | 616 | [63,65–67] |

2.1.5. $pH_{PZC}$

Figure 4 shows the $pH_{PZC}$ values of the sorbents before and after modifications by heterocyclic moiety; this was investigated using the pH-drift titration method. It was found to be close to 6.16 and 5.3, respectively, by using 0.1 M NaCl. On the other hand, the sorbents remained protonated (completely or partially) at pH less than 6.16 for MCc and 5.3 for MCa-ATA. Above this pH, the sorbents were completely deprotonated, in which the electron pairs on N, O, or S were completely available, and it was negatively charged. The pH effects and the other experiments on the sorbents (either MCc or MCa-ATA) were partially protonated (especially for MCc), and this allowed the tautomerization properties of the NH, S, and C=O for intra-rearrangements, as shown in Figure S2.

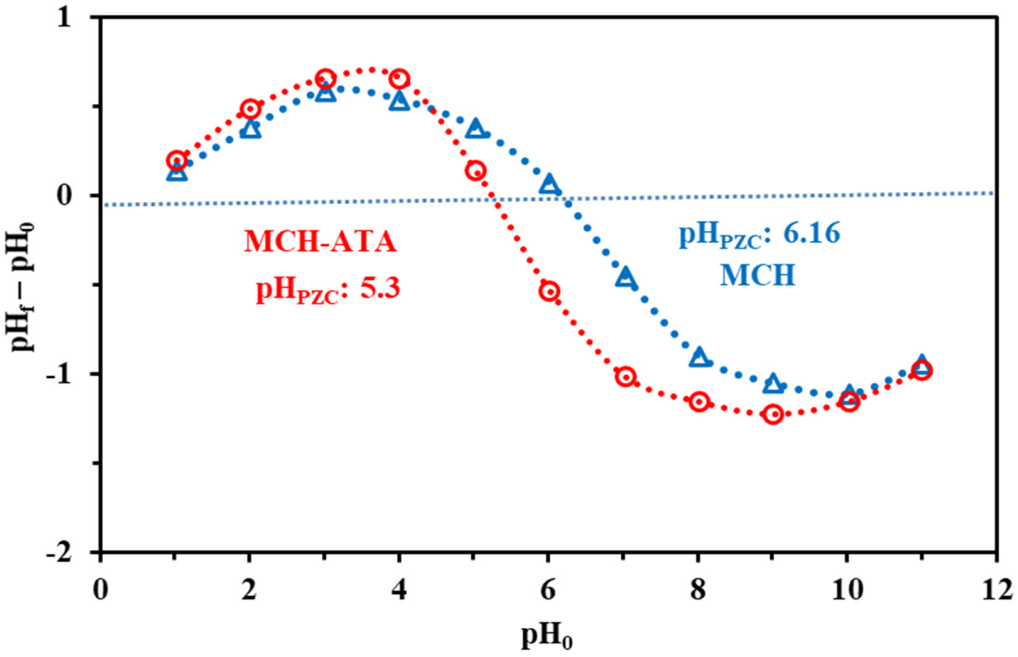


**Figure 4.** The variation of $pH_{pzc}$ of the MCc and MCa-ATA sorbents.

The $pH_{PZC}$ was influenced by the components that were used in the synthesis, in which the $pK_a$ for the amine groups in chitosan base was around 6.4–6.7. For the modified sorbent, the thiazole moiety bearing an acidic carboxylic was the main acidic characterization; the $pK_a$ of thiazole was around 2.5, while 2-amino-5-thiazole acetic acid was close to 3.2.

### *2.2. Sorption Properties*

#### 2.2.1. Effect of pH on the Sorption Properties

pH is the main parameter that had a strong impact on metal sorption in the aquatic medium associated with the metal speciation (charge of metal ions and the hydrolyzed species) and to the charge surface of the sorbent functional groups, of the physicochemical properties (as in protonation/deprotonation). Figure 5 shows the effect of the pH on the Pb(II) sorption using MCc and MCa-ATA under visible light (L) and UV in studies of photocatalytic properties. The curves have the same sorption profiles with different sorption capacities, in which at low pH values (1–3), it shows lower sorption capacities than the other pH values due to protonation of the functional groups, which make repulsion with the positively charged metal ion. This is the same with the effect of UV emission but with higher capacity. The capacity remains low at acidic pH values (i.e., for MCc, the average of both repeated experiments was around 0.0092, 0.0381, and 0.6992 mmol Pb $g^{-1}$ for the three pH values, respectively). On the other hand, the sorption was improved (reaching 0.018, 0.0545, and 0.0995 mmol Pb $g^{-1}$, respectively) under UV effect. The loading capacity for the functionalized sorbent is higher by several times, which indicated the effect of new groups for improving the sorption capacities, that reaching 0.0335, 0.0796, and 0.1454 mmol Pb $g^{-1}$, respectively, in the light and improved by using photocatalysis, but not as the same gab as the MCc sorbent, which reached 0.041, 0.1154, and 0.2087 mmol Pb $g^{-1}$, respectively, in the UV. The sorption increased by increasing the pH values until it stabilized at a pH of around 5 (before Pb(II) precipitation), which around 0.121 and 0.148 mmol Pb $g^{-1}$ for MCc in the presence of visible light and UV, respectively. On the other hand, the capacity of the functionalized sorbent reached 0.3997 and 0.5473 mmol Pb $g^{-1}$, respectively, with around four times more than the non-functionalized sorbent and almost twice by using UV catalysis.

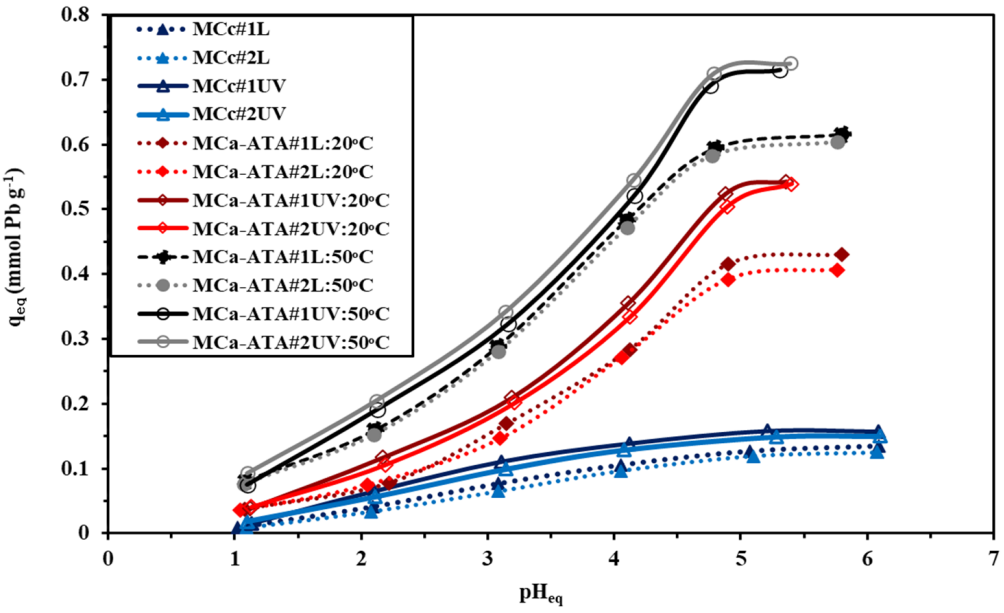


**Figure 5.** Effect of pH on the sorption performances under visible light (L) and UV for MCc and MCa-ATA sorbents.

The effect of temperature was studied either in visible light or under UV, which showed an improvement in the sorption capacities. This may be due to the effect of the temperature on the polymer network that facilitates the movement of the metal ions inside the polymer pores. The average sorption of the MCa-ATA in light and UV was around 0.586 and 0.6935 mmol Pb $g^{-1}$, respectively.

Under these experimental conditions, the sorbent was partially deprotonated and the electron pair on the ligand was available for chelating properties. The pH variations are shown in Figure S3, were less marked and reached around 0.6 units for MCc and 0.3 for MCa-ATA. It is noteworthy that the metal cation binding with protons of amine or carboxylic was varied with the pH. Figure S4 shows plotting of the $\log_{10}D$ and the equilibrium pH: the slope of the acidic medium is around +0.42, +0.47, and +0.52 for MCc, Mca-ATA at 20 °C, and MCa-ATA at 50 °C, respectively. This data emphasizes that two protons were used in ion exchange per lead ion

### 2.2.2. Uptake Kinetics

The uptake kinetics are shown in Figures 6 and S5. The studied conditions were performed at pH 5. From these Figures, it was shown that steep sorption at the first 10 min then the curve became a little slower for 20 min for MCc and 5 min for MCa-ATA. These phases were owing to the sorption on the external reactive sites that were mainly present on the surface (85% of Pb sorption from MCa-ATA and around 60% of MCc), then the second phase, which was related to the sorption on the internal reactive groups. The sorption kinetics for functionalized sorbent was faster than that of the non-modified one. The kinetics were modeled using PFORE (pseudo-first-order rate equation), PSORE (pseudo-second-order rate equation), and RID (resistance to intraparticle diffusion) equations. Table 2 reports the parameters for both MCc and MCa-ATA using visible light (L) and UV. Based on the comparison of experimental and calculated values of equilibrium sorption capacities as well as the $R^2$ values and estimated variance (EV), the PFORE fits the experimental profiles for light and UV catalysis, although the RIDE fits for both sorbents with limited extent, especially for the MCa-ATA in light.

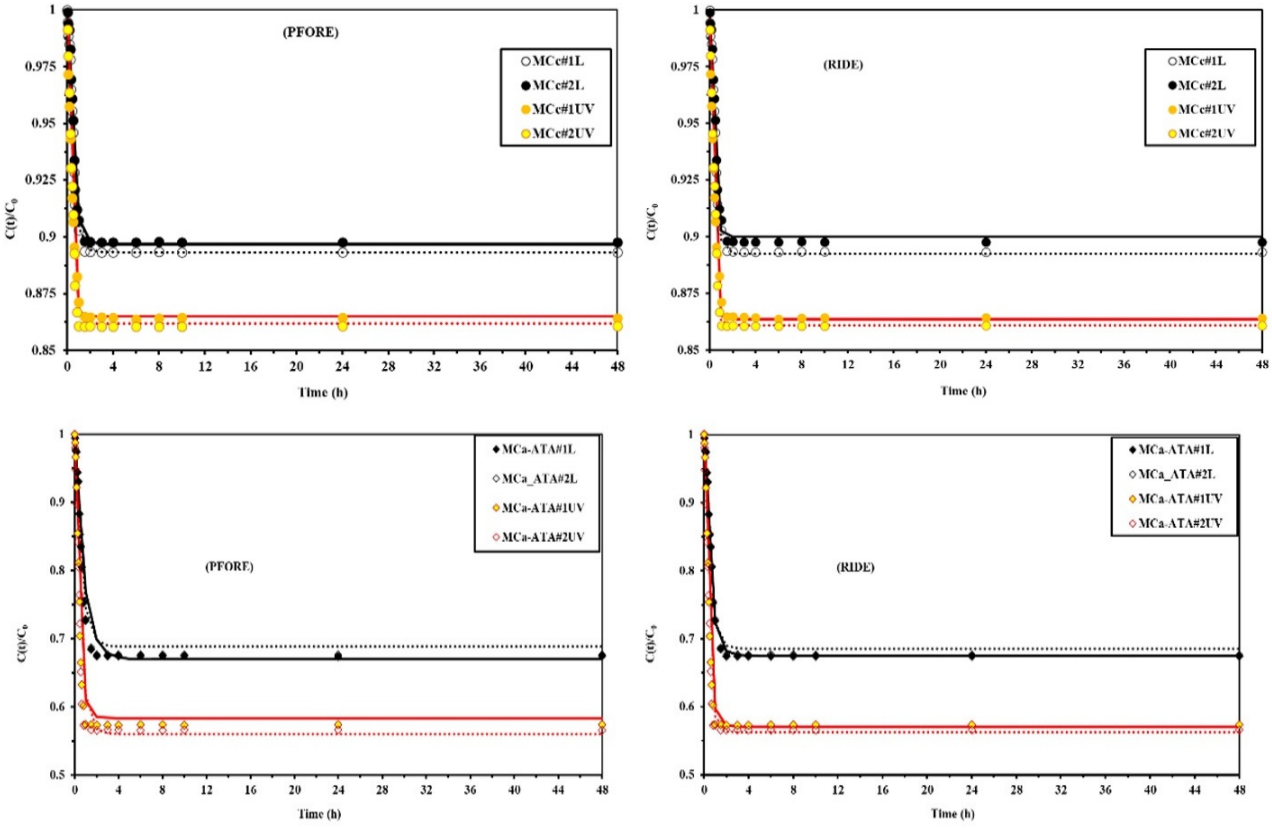


**Figure 6.** Uptake kinetics of the MCc and MCa-ATA for PFOR and RID equations under the effect of visible light and UV.

**Table 2.** Parameters of the uptake kinetics for MCc and MCa-ATA in visible light (L) and UV effect.

| | Sorbent | MCc L | | MCc UV | | MCa-ATA: L | | MCa-ATA UV | |
|---|---|---|---|---|---|---|---|---|---|
| **Model** | **Parameter Run No** | **1** | **2** | **1** | **2** | **1** | **2** | **1** | **2** |
| Exp. | $q_{eq.exp.}$ | 0.1269 | 0.1214 | 0.361 | 0.3721 | 0.3408 | 0.3398 | 0.5291 | 0.5311 |
| PFORE | $q_{eq.1}$ | 0.1302 | 0.129 | 0.367 | 0.381 | 0.3129 | 0.4897 | 0.4809 | 0.3375 |
| | $k_1 \times 10^2$ | 2.219 | 2.302 | 4.097 | 3.797 | 2.779 | 1.205 | 1.702 | 2.026 |
| | $R^2$ | 0.9574 | 0.9968 | 0.9564 | 0.9947 | 0.9564 | 0.9574 | 0.8968 | 0.99475 |
| | AIC | −83.652 | −80.405 | −64.784 | −62.387 | −30.950 | −37.349 | −48.693 | −28.257 |
| PSORE | $q_{eq.2}$ | 0.1546 | 0.178 | 0.399 | 0.399 | 0.447 | 0.407 | 0.4832 | 0.4928 |
| | $k_2 \times 10^3$ | 6.443 | 7.629 | 7.945 | 8.079 | 5.887 | 5.443 | 5.485 | 5.494 |
| | $R^2$ | 0.5023 | 0.9182 | 0.2209 | 0.1924 | 0. 7795 | 0.6964 | 0.6971 | 0.6173 |
| | AIC | −39.448 | −24.3602 | −45.2836 | −42.4199 | −29.365 | −31.938 | −27.783 | −30.678 |
| RIDE | $De \times 10^{13}$ | 1.3175 | 1.857 | 2.491 | 4.464 | 3.2285 | 3.2948 | 4.6449 | 5.1606 |
| | $R^2$ | 0.94642 | 0.93974 | 0.73732 | 0.7598 | 0.9785 | 0.9194 | 0.91527 | 0.9281 |
| | AIC | −79.673 | −72.689 | −50.259 | −55.569 | −44.959 | −40.8023 | −50.545 | −51.195 |

Simonin [68] studied the statistical effects of the experimental point distributions of the accuracy of the kinetic model and the model selection for the fitting of the experimental data. He found that points that are closed to the equilibrium orient the modeling to the PSORE against PFORE. The ionic radii of Pb(II) were around 1.19–1.2 Å [69], which is consistent with the fast kinetics, especially when most sorption is performed on the surface of the sorbent. In our case, the initial fast sorption of Pb(II) was noticed for the first 5 min for the MCa-ATA and after 10 min for MCc. In the second sorption step, it seems with a slower slope around 10 and 20 min, respectively. This is probably associated with resistance to intraparticle diffusion on the thin layer of either modified chitosan or pristine chitosan nanoparticles.

#### 2.2.3. Sorption Isotherms

Sorption isotherms were investigated at pH 5, as shown in Figures 7, 8, S6 and S7 for MCc and MCa-ATA, respectively, while Table 3 reports the parameters of the used models. It shows a steep initial slope before the equilibrium plateau. It depends on the condition used, in which the MCc in visible light and UV conditions fit the Sips equation (Figure 7), while MCa-ATA fits Langmuir and Sips but the Sips is more fitted of the experimental condition (Figure 8). The average sorption capacity of MCc was around 0.2513 mmol Pb $g^{-1}$, while for the UV condition was around 0.3466 mmol Pb $g^{-1}$ increasing by 1.25%. The MCa-ATA had an average capacity of 0.7814 mmol Pb $g^{-1}$ under visible light conditions and increased to 1.014 mmol Pb $g^{-1}$ under UV conditions.

Yang and Alexandratos [70] studied the affinity behavior of a series of sorbents bearing different chelating atoms. They concluded that the difference in sorption may be related to the Hard and Soft Acid and Base theory (so-called Pearson's rules, [71]). However, other parameters may also influence the interaction of ligands and metals as the effects of the counter-anion coordination. The complexation of the ions competes with the hydration: water coordinates of ions in the solution, which affects interaction with chelating atoms on the sorbents [70]. Marcus [72] reported that the values of hydration strengthened by −2119 kJ $mol^{-1}$ for hydration enthalpies of Pb(II) ion; this means strong hydration coordination with Pb(II). The high polarizability of the Pb(II) makes these ions preferentially bind with ligands containing N donor atoms. Giraldo et al. [73] explained the high sorption of Pb than Cu, Cd, and Zn metal ions on gelatin-activated carbon sorbent through its high ionic radius, while Yang et al. explained the better capacity of thiourea-crosslinked polystyrene toward Pb over Cd and Cu as due to the small hydrated radius [74].

Figures 7 and 8 show the most fitting model for the sorption isotherms (Sips for MCc and Langmuir and Sips for MCa-ATA sorbents). Table 3 summarizes the used parameters of the models (with the EV (estimated variances) and determination coefficients, $R^2$).

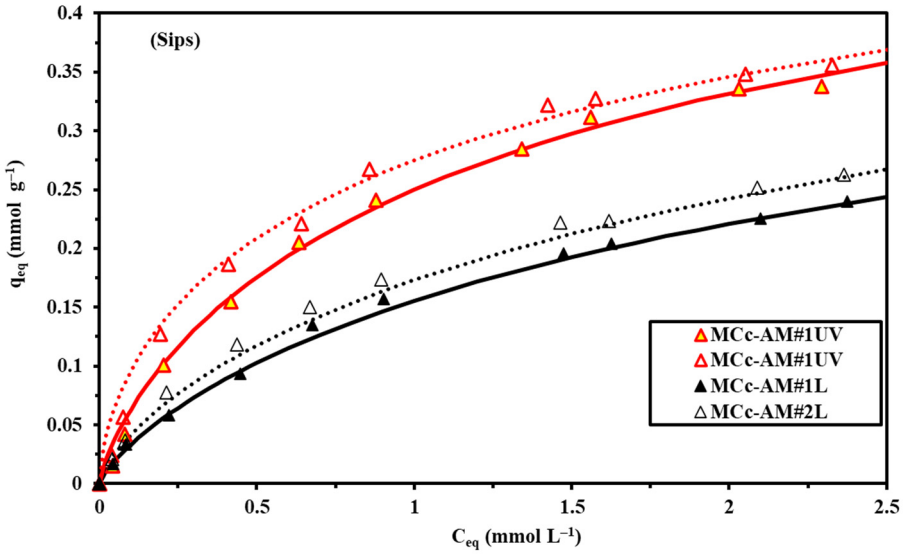


**Figure 7.** Sorption isotherms (Sips) model of the MCc sorbent under visible light and UV.

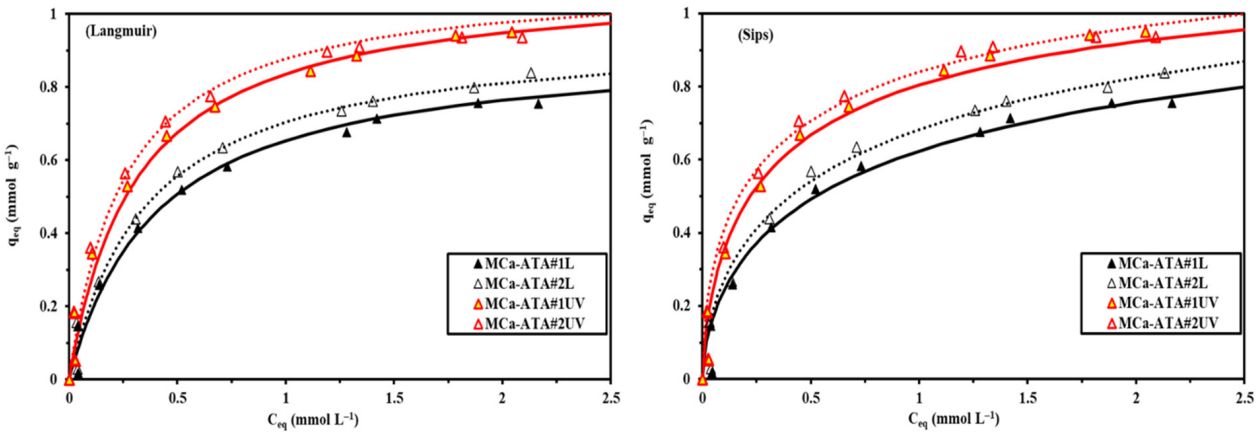


**Figure 8.** Sorption isotherms (Langmuir and Sips) model of the MCa-ATA sorbent under visible light and UV.

**Table 3.** Parameters of the sorption isotherms for MCc and MCa-ATA under visible light (L) and UV effects.

| Model | Sorbent Parameter | MCc L | | MCc UV | | MCa-ATA L | | MCa-ATA UV | |
|---|---|---|---|---|---|---|---|---|---|
| | $q_{m,exp.}$ | 0.2401 | 0.2625 | 0.3378 | 0.3554 | 0.771 | 0.7919 | 0.9754 | 0.9864 |
| Langmuir | $q_{m,L}$ | 0.319 | 0.2986 | 0.3649 | 0.3758 | 0.7513 | 0.8069 | 1.009 | 1.019 |
| | $b_L$ | 0.9942 | 0.9264 | 0.8629 | 0.9095 | 2.705 | 2.764 | 3.219 | 3.302 |
| | $R^2$ | 0.7665 | 0.8015 | 0.7947 | 0.8057 | 0.9732 | 0.9182 | 0.9263 | 0.9901 |
| | AIC | −35.706 | −32.232 | −30.166 | −29.037 | −47.537 | −49.302 | −53.389 | −53.776 |
| Freundlich | $k_F$ | 0.1634 | 0.1664 | 0.2456 | 0.2534 | 0.66854 | 0.5532 | 0.7743 | 0.8463 |
| | $n_F$ | 2.567 | 2.157 | 2.0397 | 2.1046 | 2.82796 | 2.767 | 3.68857 | 3.5486 |
| | $R^2$ | 0.7930 | 0.7300 | 0.73624 | 0.7785 | 0.86862 | 0.87226 | 0.79592 | 0.78675 |
| | AIC | −19.216 | −20.447 | −17.019 | −16.639 | −28.480 | −30.686 | −34.405 | −33.826 |
| Sips | $q_{m,S}$ | 0.2466 | 0.2857 | 0.3462 | 0.3753 | 0.7565 | 0.7994 | 1.0083 | 1.0143 |
| | $b_S$ | 0.43275 | 0.45867 | 0.68472 | 0.66221 | 0.98672 | 0.95732 | 1.8958 | 1.8674 |
| | $n_S$ | 1.2543 | 1.367 | 1.28732 | 1.2275 | 1.6549 | 1.6372 | 1.8675 | 1.9785 |
| | $R^2$ | 0.95746 | 0.92613 | 0.94752 | 0.95038 | 0.99854 | 0.99832 | 0.99898 | 0.99783 |
| | AIC | −61.282 | −60.998 | −56.495 | −55.978 | −68.969 | −70.056 | −58.948 | −56.406 |

Table 4 reports the sorption behavior of sorbents for Pb(II) and compare the capacity with the synthesized composites. However, this comparison is difficult due to the unsystematic approach of the experiments that were not carried out under similar conditions. Some synthetic sorbents showed a higher sorption affinity, e.g., the thiourea-modified with polystyrene resin [74] or HA-MG-CH, but the most advantage and promising of this sorbent was the fast kinetics, where around 15 min was sufficient for complete sorption.

**Table 4.** Comparison of sorption properties for sorbents (conventional) and bio-sorbents.

| Sorbent | pH | $t_{eq}$ (min) | $q_m$ (mmol $g^{-1}$) | Reference |
|---|---|---|---|---|
| Sulphurized carbon activated | 5.4 | - | ≈0.3 | [75] |
| Chlamydomonas-reinhardtii/alginate | 6.0 | 90 | 1.84 | [76] |
| Magnetic biochar (oak bark) | 5.0 | 60 | 0.146 | [77] |
| Sugarcane-bagasse | 5.0 | 60 | 0.0054 | [78] |
| Beet-pulp | 5.0 | 60 | 00090 | [78] |
| Silica coated magnetic-nanosorbent functionalized with mercaptoamine | 6–7 | 120 | 1.41 | [79] |
| Thiamine/silica | 5.0 | 120 | 0.19 | [80] |
| Hydroxamic-acid/amidoxime bi-functional acrylic acid sorbent | - | - | 0.94 | [81] |
| Schiff-base sorbent | 10 | 120 | 0.50 | [82] |
| Purolite-C100 sorbent | 5-6 | 1440 | 0.046 | [83] |
| Modified Amberlite/XAD-16 sorbent | - | 60 | 0.519 | [84] |
| Di (2-ethylhexyl) phosphate sorbent | 4 | 80 | 0.172 | [85] |
| Gelatin activated carbon | 5 | 60 | 1.79 | [86] |
| Thiourea hyper-crosslinked with polystyrene resin | 6.0 | | 3.33 | [74] |
| Salicylic acid-formaldehyde-catechol sorbent | 6.0 | 240 | 0.931 | [87] |
| Tripolyphosphate-chitosan | 5.0 | 1080 | 1.21 | [73] |
| Azido-fiber | 6.0 | 1440 | 1.50 | [88] |
| HA-MG-CH | 5.0 | 60 | 2.51 | [39] |
| CHI-L | 5.0 | 35 | 0.2513 | This work |
| CHI-UV | 5.0 | 30 | 0.3466 | This work |
| CHI-ATA-L | 5.0 | 20 | 0.7814 | This work |
| CHI-ATA-UV | 5.0 | 15 | 1.014 | This work |

#### 2.2.4. Metal Desorption and Sorbent Recycling

Not only the sorption properties are taken into account for the evaluation of the competitiveness of sorption processes, but also the efficiency of the metal recoveries and the recycling effectiveness of the sorbent. Logically, weakly acid solutions have been investigated for these parameters. To avoid sorbent degradation, a diluted HCl (0.2 M) solution is used for metal desorption investigation.

To evaluate desorption kinetics and the required time for full desorption, preliminary studies were performed (Figure 9). A few minutes of contact with 0.2 M HCl were sufficient for more than 98% desorption, while full desorption was achieved after a longer contact time (around 10–15 min for MCa-ATA and around 30 min for MCc). These experiments were also performed in the presence and absence of UV. Figure 9 shows the effect of UV on the desorption as was happened for improving sorption behaviors; this experiment was performed through the sorbents from the kinetic experiments.

Table 5 compares the average of sorption/desorption values efficiencies and the Pb(II) sorption capacities using both of sorbents in the presence and absence of UV for five cycles. A small (limited) loss was shown in the sorption capacities during the five cycles, and the loss in the case of MCc was more than that of the modified sorbent, while the average in the presence of visible light was much higher than in UV. However, the decreases (totally) reached up to 10% for Pb(II) in MCc and around 3% for MCa-ATA, while the average of desorption during the five cycles was around 99.5% (±0.3%). This means that both sorption/desorption performances for a minimum of five cycles were remarkably stable and the Pb(II) metal ions were desorbed effectively by 0.2 M HCl solution with a loss in the desorption efficiency for long cycle terms.

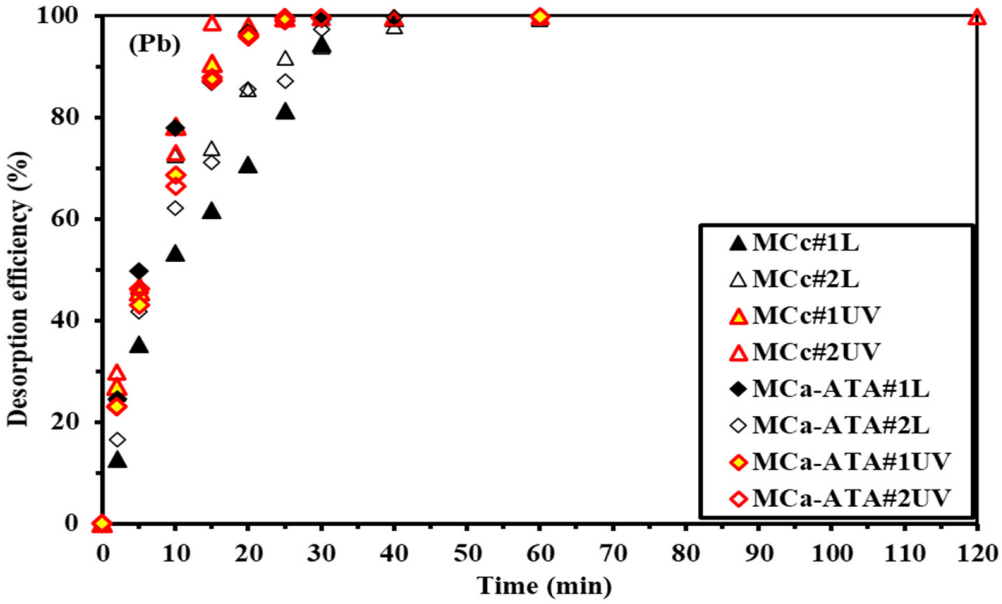


**Figure 9.** Desorption kinetics of the MCc and MCa-ATA from 0.2 M HCl solution under visible light (L) and UV.

**Table 5.** Sorption desorption cycles of MCc and MCa-ATA for five cycles using 0.2 M HCl solution.

| | MCc | | MCa-ATA | |
|---|---|---|---|---|
| | **SORPTION** | **DESORPTION** | **SORPTION** | **DESORPTION** |
| Cycles | q mg $g^{-1}$ | Des % | q mg $g^{-1}$ | Des % |
| 1 | 35.0260 | 100.00 | 110.646 | 100.00 |
| 2 | 34.156 | 99.99 | 109.589 | 100.00 |
| 3 | 33.125 | 99.98 | 109.391 | 99.98 |
| 4 | 32.099 | 99.961 | 108.383 | 99.94 |
| 5 | 31.466 | 99.82 | 107.089 | 99.89 |
| Loss% | 10.164% | 0.18% | 3.215 | 0.11% |

2.2.5. Tests on a Complex Multi-Metal Sample

For the evaluation performance of the sorption system, it is necessary to investigate the sorption from a complex solution (i.e., multi-metallic simulated to the real effluents). The sorption capacities and performances, as well as the distribution coefficients ($K_d$, L $g^{-1}$) of MCa-ATA, is investigated at different pH 2–5 for 5 h. It was shown that the sorption performance is improved with the pH, the capacity increased by increasing pH values. The complexity of the solution (multi-metal concentration) explains the marked effect of the sorption performance toward metal ions, which is the interest. It was shown that the high removal efficiency was in the order of Pb(II), Fe(III), Nd(III), Zn(II), Al(III), Mg(II), and Ca(II). The comparison of the distribution coefficients was in terms of Pb(II) > Fe(III) ≈ Zn(II) > Nd(III) > Al(III) > Mg(II) > Ca(II). The Pb(II), Fe(III), and Zn(II) ions are considered as borderline acids, while Al(III), Nd(III), Ca(II), and Mg(II) are considered as hard acids. These two classification groups have a high affinity for the N containing functional groups. A selectivity coefficient $SC_{Pb/metal}$ was shown in Figure 10. It is defined by the mass balance equation as follows $K_{d(Pb)}/K_{d(metal)}$. The preference of the MCa-ATA for Pb(II) over other metals is relatively high, especially at the alkaline pH values.

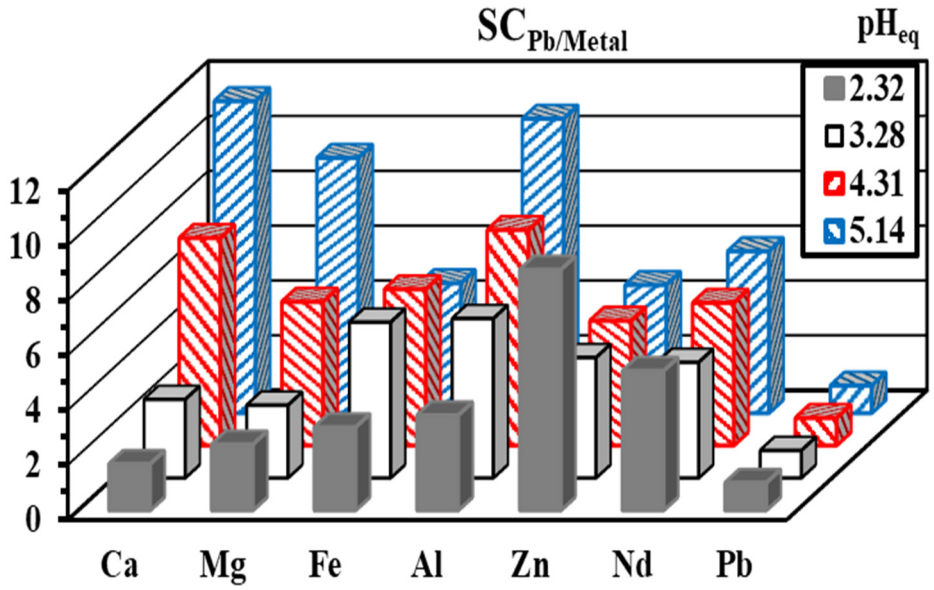


**Figure 10.** Selectivity coefficient of MCa-ATA for Pb over the other associated elements in polymetallic solution.

### *2.3. Treatment of Nature Effluent*

The natural effluent was obtained from the Ramlet Hemeyir, which lies in the southwestern Sinai-Egypt, (i.e., 72 km to the southeast of the city of Abu Zenima), between latitudes 29° 0/–29° 2/N and longitudes 33° 30/–33° 33/E (Figure S8). Due to the highly ferruginous properties of this area, especially in the Adedia Formation (with a thickness of 72 m), it is stained by iron oxyhydroxides and manganese. The top part of this Formation consists of ferruginous siltstone, ferruginous sandstone, and lateritization mainly of iron with less alumina, which makes this section of red ferruginous clay. Several overlapping formations were noticed in this area of the Adedia Formation and Um Bogma Formation. This locality is characterized by phosphate minerals such as wavellite $Al_3(PO_4)_2(OH)_2.5H_2O$, xenotime ($YPO_4$), vivianite $Fe_3(PO_4)_2.8H_2O$, and saleeite $Mg(UO_2)_2(PO_4)_2.H_2O$, also others were identified, i.e., euxenite (Y,Ca,Ce,U,Th) $(Nb,Ta,Ti)_2O_6$, becquerelite ($CaU_6O_{19}.11H_2O$), rutile ($TiO_2$), hematite ($Fe_2O_3$), goethite (αFeO)(OH) ilmenite ($FeTiO_3$), and quartz ($SiO_2$). Table S3 shows the chemical composition of the pristine ore materials before chemical treatment.

One Kg of ground ore material (around 1 cm) was agitated in 3 L of 200 g $L^{-1}$ sulfuric acid solution for 3 h at 150 (±10) °C. The produced liquor (around 2300 mL) was applied for the extraction process. Table S4 shows the contents of the leaching liquor and the effluent after treatment.

Series of extraction processes were applied for the recovery of uranium (using the Amberlite IRA-400 at pH of around 2), REE (by using (DOWEX 50 resin at pH of around 4) after Fe(III) precipitation. The produced effluent was still contaminated by Pb(II) and a small ratio of U and REE. Table S4 shows the effluent contents of the most important metal ions. The sorption was achieved with the batch method at pH 5 under visible light and UV effect.

Figure S9 shows the removal efficiency percent of metal ions in the treated effluents; it has the order of Pb, U, Al, Fe, Ni, REE, Si, Ca, Mn with removal percentages of 50.36, 38.67, 29.38, 24.08, 11.99, 5.31, 4.65, 4.11, and 3.03%, respectively, in light condition, while in the UV condition, it was noticed that; (a) the same order of visible light but with increasing the ratios and (b) the affinity for Ca was much more than Si (61.45, 50.49, 43.77, 28.34, 21.02, 9.16, 7.09, 7.33, and 5.74%, respectively). Figure 11 shows the selectivity coefficient of the sorbent toward metal ions at pH 5 in light and under UV emission. The order of selectivity set as the following order Ca > REE > Si > Mn > Ni > Fe > Al > U in light condition, while in the SC under the effect of UV is as follow Ca ≈ Si > REE > Mn > Ni > Fe > Al > U.

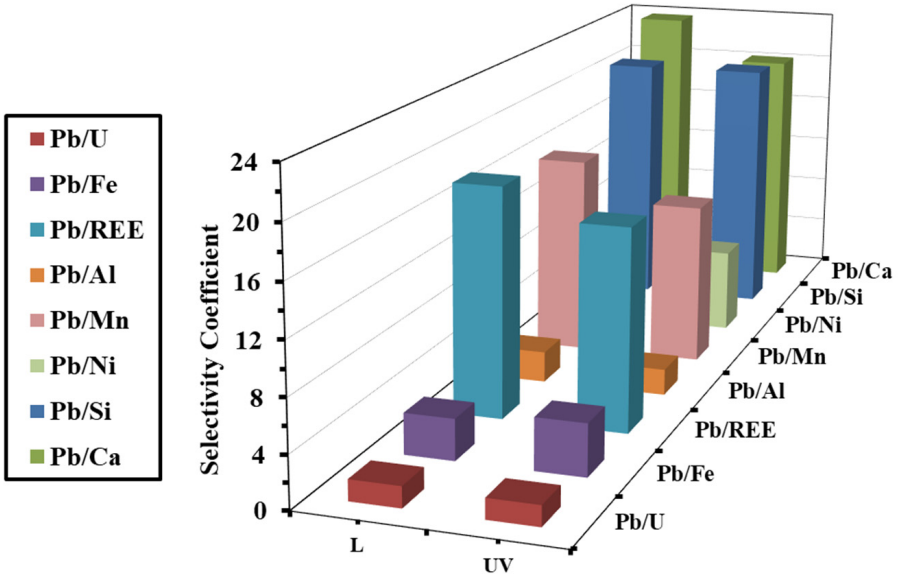


**Figure 11.** Selectivity coefficient of MCa-ATA under visible light (L) and UV conditions.

## 3. Materials and Methods

### *3.1. Materials*

Sodium bisulfite, ~40%, formaldehyde 36.5–38% in $H_2O$, 2-Amino-4-thiazoleacetic acid, chitosan (25% degree of acetylation, DA), epichlorohydrin (EPI) 98%, urea > 99%, NaOH anhydrous ≥ 98%, calcium chloride anhydrous > 97%, glutaraldehyde solution (25% *w*/*w*), and sodium nitrite ≥ 99.0% were supplied from Sigma Aldrich (Merck KGa, Darmstadt, Germany). Neodymium sulfate was provided by the National Engineering Research Centre of Rare Earth Metallurgy and Functional Materials Co., Ltd. (Baotou, China). $MgCl_2{\cdot}6H_2O$, $AlCl_3{\cdot}6H_2O$, $CuSO_4$, and $ZnCl_2$ were obtained from Guangdong Guanghua, Sci-Tech Co., Ltd. (Guangdong, China).

### *3.2. Preparation Sorbents*

#### 3.2.1. Preparation of Magnetite Nanoparticles

Thermal co-precipitation, which is known as the Massart [89] method, was used for preparing the nanoparticles. This was performed by the dissolution of a mixture of hydrated ferrous sulfate ($FeSO_4.7H_2O$; 5.0 g, 18.18 mmol) and ammonium ferric sulfate ($(NH_4)Fe(SO_4)_2.12H_2O$; 17.35 g, 35.98 mmol) in the water medium. The reaction was maintained at 40–50 °C for 60 min (under vigorous stirring); the magnetite (precipitation) was performed by adjusting pH to 10–12 value using 5 M NaOH, while continued stirring for 5 h at 45 °C. The magnetite nanoparticles were magnetically separated, washed by distilled water/acetone, and dried at 50 °C for 20 h.

#### 3.2.2. Preparation of Magnetite Chitosan Nanoparticles

Chitosan particles (4 g) were dissolved in a solution of 150 mL 7% acetic acid (AA) solution, 2 g of dried magnetite nanoparticles was added to the solution. The pH was adjusted to 10 by 5 M NaOH solution, while the temperature was maintained as fixed to 45 °C for the precipitation of chitosan nanoparticles. The temperature was raised to 90 °C with stirring for 3 h. The produced precipitated particles (MC, 5.8 g) were separated using magnetic control then washed with distilled water and acetone for the next step. This step was used for enhancing the stability of the composites by crosslinking procedure, the alkaline solution of 0.01 M epichlorohydrin (EPI), mixed with 0.067 M NaOH solution; the pH of the solution is set to 10. The temperature of the reaction was adjusted to 60 ± 3 °C for 3 h. The product was magnetically separated (MCc, 5.83 g) followed by rinsing with acetone and water before being dried at 50 °C for 20 h (Scheme 1).

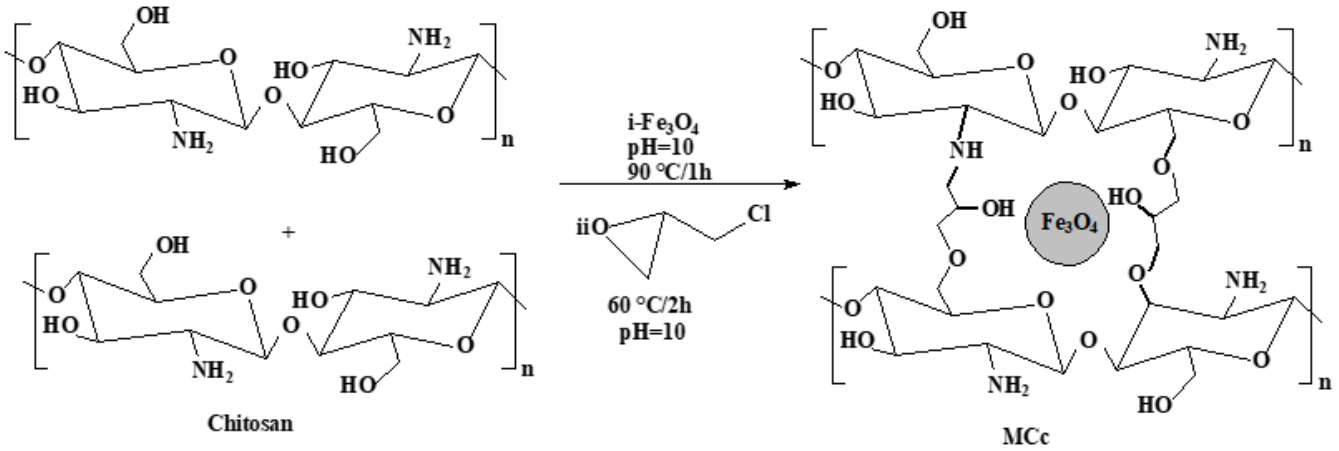


**Scheme 1.** Synthesis route for the magnetite chitosan nanoparticles.

### 3.2.3. Synthesis of the Activated Spacer Arm

The produced crosslinked magnetite chitosan particles were applied for further reaction to produce an activated side using EPI in ethanol medium. The reaction was performed by mixing the crosslinked chitosan particles with 18 mL (164.8 mmol) EPI in a 150 mL ethanolic solution (ethanol/water (1:1/*v*:*v*)). The reaction was refluxed at 70 °C for 3 h. The produced chlorinated materials (activated chitosan (MCa, 8.8 g)) were separated from the solution using the magnetic control, washed with ethanol and water, then dried for 20 h at 50 °C (Scheme 2).

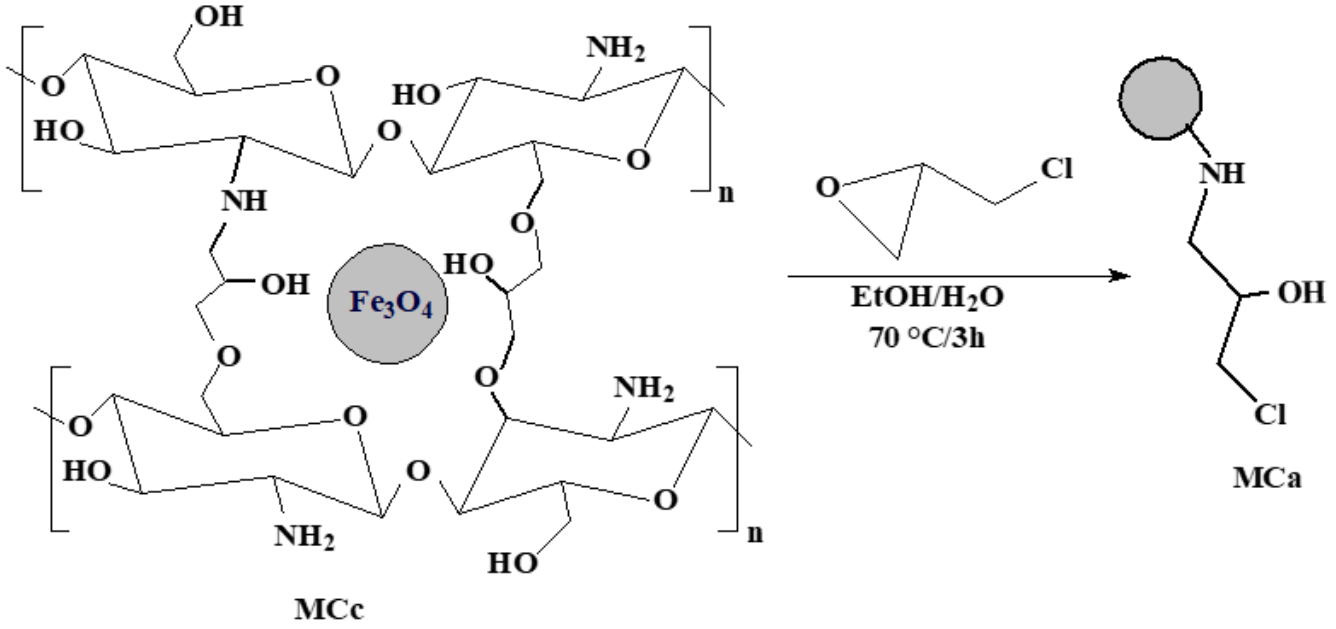


**Scheme 2.** Synthesis route of the activated spacer arm magnetite chitosan nanoparticles.

### 3.2.4. Grafting of Amine Thiol Derivative

Five grams of amine thiazole derivative (31.6 mmol) were dissolved in 150 mL DMF. The pH of this solution was adjusted to 10 by NaOH solution (5 M). The temperature was elevated to 85 °C after the addition of 6 g activated chitosan with continuous stirring for 10 h. The produced precipitate (functionalized chitosan nanoparticles) was magnetically separated and rinsed several times with ethanol and water before being dried at 50 °C for 24 h (Scheme 3).

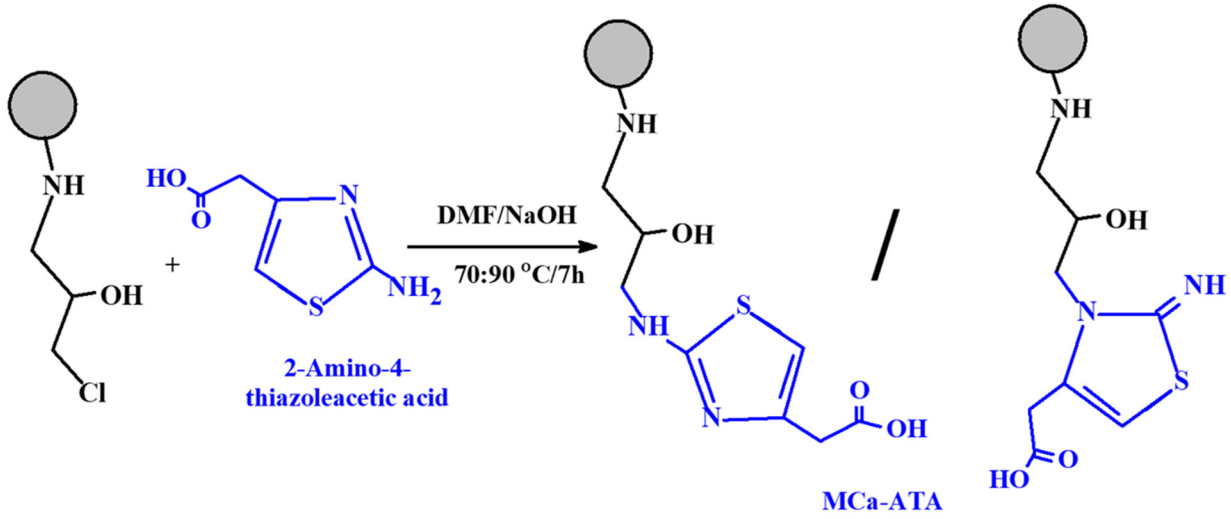


**Scheme 3.** Synthesis route of the modified thiazole derivative of the magnetite chitosan nanoparticles.

### *3.3. Sorbent Characterization*

FT-IR spectroscopy was used for functional groups' identification and elucidating of the sorbent structure; the dried samples were designed as KBr disc then analyzed using IRTracer-100-FT-IR (Shimadzu, Tokyo, Japan) after grinding and mixing well. The particle size with the morphology structure of the prepared sorbent was analyzed by TEM analysis (transmission electron microscopy) JEOL-1010 (JEOL, Ltd., Tokyo, Japan). The SEM morphologies were obtained by Phenom-ProX-SEM (Thermo Fisher Scientific, Eindhoven, The Netherlands). Element contents of the sorbent composition (before and after loading with metal ions) were performed by semi-quantitative EDX analysis. The drift method [90] was used for the determination of the pH zero charge ($pH_{pzc}$). Thermally decomposition of the sorbent was performed by TGA analysis by Netzsch-STA, 449-F3 Jupiter (NETZSCH, Gerätebau, HGmbh, Selb, Germany), the sample weight is around ~1.978 and 2.64 mg for MCc and MCa-ATA respectively, it is occurred in aluminum crucibles at a temperature of around 30 to 800 °C, under nitrogen atmosphere for temp. ramp 10 °C $min^{-1}$, it was performed under nitrogen atmosphere for temp. ramp 10 °C $min^{-1}$. Adjusting the pH of the solution in the experiments by compact pH ionometer S220-Seven, Mettler, Toledo, (Shanghai, China), the samples were collected from solutions before and after loading for determination using ICP-AES (inductively coupled plasma atomic emission spectrometer) with model ICPS 7510 (Shimadzu, Tokyo, Japan) after filtration using a membrane. Porosity and surface area were measured through nitrogen adsorption/desorption isotherms by Micromeritics-TriStar II, Norcross-GA system 77 K (USA). The samples were swept firstly under nitrogen for 5 h at 110 °C.

### *3.4. Sorption Tests*

The batch system was used for describing the sorption tests. A volume of solution ($V$, L) with fixed initial metal concentration ($C_0$, mmol $L^{-1}$) at initial pH ($pH_0$) was agitated (210 rpm), with a fixed amount of sorbent ($m$, g) at 20 ± 1 °C temperature ($T$) for 24 h under visible light (L) and UV emission. After sorption, the samples were filtered and the residual metal concentration ($C_{eq}$; mmol $L^{-1}$) was analyzed using the ICP tools. Uptake kinetics were homogeneously agitated at a given time, analyzed after filtration. The loading capacity ($q_{eq}$, mmol $g^{-1}$) was determined using the mass balance equation: $q_{eq} = (C_0 - C_{eq}) \times V/m$. The PFORE (pseudo-first-order rate equation), PSORE (pseudo-second-order rate equation), and RIDE (resistance to intraparticle diffusion; so-called Crank equation) were used for fitting the models as represented in Table S5a, (see Supplementary Information). The isotherm models (Langmuir, Sips, and Freundlich equations) are represented as the modeling of isotherms, which are reported in Table S5b. The effect of associated metal ions

was discussed as a function of selectivity, the choice of these elements depending upon that familiar presence in the solution (nature solution and leachate liquor); this experiment was discussed with equimolar amounts of metal ions at different pH values for study the selectivity ratio at differing conditions.

Desorption experiments were discussed depending on kinetics, the sorption desorption recycling steps (rinsing with water after each cycle), and the desorption process was calculated using the mass balance equation. Each experiment was repeated twice for reproducibility under both visible light and UV effects.

### *3.5. Recovery of Pb from Raffinate Solution*

The metal ions concentration in the ore material was analyzed after dissolution using different acid types (HF, $HNO_3$, and HCl). A fixed amount (0.5 g) was digested with HF in a Teflon beaker at 150 °C for silica digestion. After evaporating and dryness, another round began with $HNO_3$ and HCl for dissolving of the minerals, with a few drops of peroxide for organic digestion. The final amount was diluted to 100 mL for measuring the major and trace elements [91–93]. The metal content is reported in Table 1.

The ore material undergoes mild leaching using 200 g $L^{-1}$ at 150 °C for 3 h with S/L ratio of 1/3. The produced leaching solution was investigated and reported in Table 2. The yield solution was applied for recovering U and REE using anionic exchange resin amberlite IRA400 and cationic exchange resin DOWEX 50X8, respectively. The yield solution was applied on this sorbent for metal recovery.

## 4. Conclusions

Successive grafting of the heterocyclic base of thiazol moiety on chitosan nanoparticles enhanced sorption efficiency toward Pb(II). The sorbent was characterized by FTIR, EA, SEM and SEM-EDX, XRD, TEM, and BET surface area through the nitrogen sorption desorption effect. The sorbent shows a particle size of around 10 nm, which limits the intraparticle diffusion properties. The sorption capacities were performed under visible light and UV emission for the pristine chitosan magnetite nanoparticles (MCc) and functionalized sorbent (MCa-ATA). The UV improves the sorption performances (capacity and kinetics) of both sorbents. Fast kinetics of the modified sorbent around 15 min for full saturation compared to 30 min for the MCc sorbent. From the sorption profiles of both MCa-ATA and MCc, it was shown that the higher performance of MCa-ATA over MCc (0.251 and 0.346 mmol Pb $g^{-1}$ in visible light and under UV, respectively, for MCc compared to 0.7814 and 1.014 mmol Pb $g^{-1}$, respectively, for the MCa-ATA in the same conditions. The sorption profiles of both sorbents show the high kinetics of MCa-ATA (15 min) over MCc (20 min sufficient for complete sorption). The 85% of Pb(II) sorption was achieved in the first 10 min for MCa-ATA compared to 60% for the MCc. The MCa-ATA is highly efficient for the treatment of contaminated solutions (including water). From the sorption/desorption experiments, it was shown that the sorbent is chemically stable with fast desorption profile. The sorbent shows a preference for Pb over representative elements, while less selectivity is obtained compared to Fe and U. It is a promising sorbent for recovering of heavy metal ions as well as the removal of contaminants in polymetallic solution at high pH values under UV emission and used in a wide range of pH.

**Supplementary Materials:** The following supporting information can be downloaded at: https://www.mdpi.com/article/10.3390/catal12030330/s1, Figure S1: TGA and Dr-TGA of MCc (a) and MCa-ATA (b); Figure S2. Tautomerization of the functionalized sorbent in a mild pH condition; Figure S3: pH variation of MCc and MCa-ATA at 20 and 50 °C under light and UV effect; Figure S4: The data collected from plotting of the log10D and the equilibrium pH; Figure S5: Sorption kinetics of MCc and MCa-ATA for the PSORE at light and UV effect; Figure S6: Sorption Isotherms (Langmuir and Freundlich) models of the MCc sorbent at light and UV; Figure S7: Sorption Isotherms (Freundlich) model of the MCa-ATA sorbent at light and UV; Figure S8: Geological map of the studied area; Figure S9: Removal efficiency precent of metal ions in the ore effluent after treatment with MCa-ATA under light and UV conditions. Table S1: Diffraction patterns of the XRD peaks and the matched

reference file. Table S2: Elemental analysis of MCc and MCa-ATA sorbents; Table S3: Chemical composition of the ferruginous sandstone ore material; Table S4: Chemical composition of the ore leachates and the produced effluents after extraction treatments; Table S5a: Reminder on equations used for modeling uptake kinetics [94–96]; Table S5b: Reminder on equations used for modeling sorption isotherms [95,97,98]. References [94–99] are cited in the supplementary materials.

**Author Contributions:** Conceptualization, and methodology M.F.H., Y.W. and A.F.; software, and formal analysis M.F.H., A.A.-H.A.-R. and H.H.A.; investigation and resources, M.F.H., S.N. and T.F.; data curation, S.H.A., A.E.-S.G., H.I.M. and S.N.; writing, review, and editing, A.F. and M.F.H.; project administration, S.H.A., H.H.A., S.N. and Y.W.; funding acquisition, S.H.A., H.H.A., S.N. and Y.W. All authors have read and agreed to the published version of the manuscript.

**Funding:** Taif University for Researchers Supporting Project (TURSP-2020/83), Taif University, Taif, Saudi Arabia. National Natural Science Foundation of China [22066005, U1967218, 11975082] and NSFC 21976039.

**Institutional Review Board Statement:** Not applicable.

**Informed Consent Statement:** Not applicable.

**Data Availability Statement:** Data are available from authors.

**Acknowledgments:** We acknowledge Taif University for the Researchers Supporting Project number (TURSP-2020/83), Taif University, Taif, Saudi Arabia. Y.W., S.N. and T.F. appreciate the Natural Science Foundation of China, grant numbers [22066005, U1967218, 11975082] and NSFC 21976039.

**Conflicts of Interest:** The authors declare no conflict of interest.

## References

1. Yaseen, D.; Scholz, M. Textile dye wastewater characteristics and constituents of synthetic effluents: A critical review. *Int. J. Environ. Sci. Technol.* **2019**, *16*, 1193–1226. [CrossRef]
2. Fouda, A.; Hassan, S.E.-D.; Abdel-Rahman, M.A.; Farag, M.M.S.; Shehal-deen, A.; Mohamed, A.A.; Alsharif, S.M.; Saied, E.; Moghanim, S.A.; Azab, M.S. Catalytic degradation of wastewater from the textile and tannery industries by green synthesized hematite ($\alpha$-$Fe_2O_3$) and magnesium oxide (MgO) nanoparticles. *Curr. Res. Biotechnol.* **2021**, *3*, 29–41. [CrossRef]
3. Mashaal, N.; Akagi, T.; Ishibashi, J. Hydrochemical and isotopic study of groundwater in Wadi El-Natrun, Western Desert, Egypt: Implication for salinization processes. *J. Afr. Earth Sci.* **2020**, *172*, 104011. [CrossRef]
4. Saied, E.; Eid, A.M.; Hassan, S.E.; Salem, S.S.; Radwan, A.A.; Halawa, M.; Saleh, F.M.; Saad, H.A.; Saied, E.M.; Fouda, A. The Catalytic Activity of Biosynthesized Magnesium Oxide Nanoparticles (MgO-NPs) for Inhibiting the Growth of Pathogenic Microbes, Tanning Effluent Treatment, and Chromium Ion Removal. *Catalysts* **2021**, *11*, 821. [CrossRef]
5. Fouda, A.; Hassan, S.E.-D.; Saied, E.; Azab, M.S. An eco-friendly approach to textile and tannery wastewater treatment using maghemite nanoparticles ($\gamma$-$Fe_2O_3$-NPs) fabricated by Penicillium expansum strain (Kw). *J. Environ. Chem. Eng.* **2021**, *9*, 104693. [CrossRef]
6. Sana, Y.; Hina, R. Irrigation of Zea mays with UASB-treated textile wastewater; effect on early irrigation of Zea mays with UASB-treated textile wastewater; effect on early growth and physiology. *Environ. Sci. Pollut. Res. Int.* **2020**, *27*, 15305–15324.
7. Daud, M.; Rizvi, H.; Akram, M.F.; Ali, S.; Rizwan, M.; Nafees, M.; Jin, Z.S. Review of upflow anaerobic sludge blanket reactor technology: Effect of different parameters and developments for domestic wastewater treatment. *J. Chem.* **2018**, *2018*, 1596319. [CrossRef]
8. Salem, S.S.; Mohamed, A.; El-Gamal, M.; Talat, M.; Fouda, A. Biological decolorization and degradation of azo dyes from textile wastewater effluent by Aspergillus niger. *Egypt. J. Chem.* **2019**, *62*, 1799–1813.
9. Kong, L.J.; Zhang, H.M.; Ji, W.; Shih, K.M.; Su, M.H.; Diao, Z.H.; Xu, R.M.; Hou, L.A.; Song, G.; Chen, D.Y. Recovery of phosphorus rich krill shell biowaste for uranium immobilization: A study of sorption behavior, surface reaction, and phase transformation. *Environ. Pollut.* **2018**, *243*, 630–636. [CrossRef]
10. Guilhen, S.N.; Rovani, S.; Araujo, L.G.d.; Tenório, J.A.S.; Mašek, O. Uranium removal from aqueous solution using macauba endocarp-derived biochar: Effect of physical activation. *Environ. Pollut.* **2021**, *272*, 116022. [CrossRef]
11. Nasrollahzadeh, M.; Sajjadi, M.; Iravani, S.; Varma, R.S. Starch, cellulose, pectin, gum, alginate, chitin and chitosan derived (nano) materials for sustainable water treatment: A review. *Carbohydr. Polym.* **2021**, *251*, 116986. [CrossRef] [PubMed]
12. Guibal, E. Interactions of metal ions with chitosan-based sorbents: A review. *Sep. Purif. Technol.* **2004**, *38*, 43–74. [CrossRef]
13. Gao, X.; Guo, C.; Hao, J.; Zhao, Z.; Long, H.; Li, M. Adsorption of heavy metal ions by sodium alginate based adsorbent—A review and new perspectives. *Int. J. Biol. Macromol.* **2020**, *164*, 4423–4434. [CrossRef] [PubMed]
14. Sutirman, Z.A.; Sanagi, M.M.; Aini, W.I.W. Alginate-based adsorbents for removal of metal ions and radionuclides from aqueous solutions: A review. *Int. J. Biol. Macromol.* **2021**, *174*, 216–228. [CrossRef] [PubMed]
15. Zhou, L.; Zou, H.; Wang, Y.; Liu, Z.; Le, Z.; Huang, G.; Luo, T.; Adesina, A.A. Immobilization of in situ generated Fe-0-nanoparticles in tripolyphosphate-crosslinking chitosan membranes for enhancing U(VI) adsorption. *J. Radioanal. Nucl. Chem.* **2017**, *311*, 779–787. [CrossRef]

16. Huang, Z.; Li, Z.; Zheng, L.; Zhou, L.; Chai, Z.; Wang, X.; Shi, W. Interaction mechanism of uranium(VI) with three-dimensional graphene oxide-chitosan composite: Insights from batch experiments, IR, XPS, and EXAFS spectroscopy. *Chem. Eng. J.* **2017**, *328*, 1066–1074. [CrossRef]
17. Tang, X.; Zhou, L.; Le, Z.; Wang, Y.; Liu, Z.; Huang, G.; Adesina, A.A. Preparation of porous chitosan/carboxylated carbon nanotube composite aerogels for the efficient removal of uranium(VI) from aqueous solution. *Int. J. Biol. Macromol.* **2020**, *160*, 1000–1008. [CrossRef]
18. Hamza, M.F.; Wei, Y.; Benettayeb, A.; Wang, X.; Guibal, E. Efficient removal of uranium, cadmium and mercury from aqueous solutions using grafted hydrazide-micro-magnetite chitosan derivative. *J. Mater. Sci.* **2020**, *55*, 4193–4212. [CrossRef]
19. Hamza, M.F.; Gamal, A.; Hussein, G.; Nagar, M.S.; Abdel-Rahman, A.A.H.; Wei, Y.; Guibal, E. Uranium(VI) and zirconium(IV) sorption on magnetic chitosan derivatives—Effect of different functional groups on separation properties. *J. Chem. Technol. Biotechnol.* **2019**, *94*, 3866–3882. [CrossRef]
20. Selim, M.T.; Salem, S.S.; Mohamed, A.A.; El-Gamal, M.S.; Awad, M.F.; Fouda, A. Biological treatment of real textile effluent using Aspergillus flavus and Fusarium oxysporium and their consortium along with the evaluation of their phytotoxicity. *J. Fungi* **2021**, *7*, 193. [CrossRef]
21. Eid, A.M.; Fouda, A.; Niedbała, G.; Hassan, S.E.-D.; Salem, S.S.; Abdo, A.M.; Hetta, H.F.; Shaheen, T.I. Endophytic Streptomyces laurentii mediated green synthesis of Ag-NPs with antibacterial and anticancer properties for developing functional textile fabric properties. *Antibiotics* **2020**, *9*, 641. [CrossRef] [PubMed]
22. Mohamed, A.A.; Fouda, A.; Abdel-Rahman, M.A.; Hassan, S.E.-D.; El-Gamal, M.S.; Salem, S.S.; Shaheen, T.I. Fungal strain impacts the shape, bioactivity and multifunctional properties of green synthesized zinc oxide nanoparticles. *Biocatal. Agric. Biotechnol.* **2019**, *19*, 101103. [CrossRef]
23. Fouda, A.; Eid, A.M.; Abdel-Rahman, M.A.; EL-Belely, E.F.; Awad, M.A.; Hassan, S.E.-D.; AL-Faifi, Z.E.; Hamza, M.F. Enhanced Antimicrobial, Cytotoxicity, Larvicidal, and Repellence Activities of Brown Algae, *Cystoseira crinita*-Mediated Green Synthesis of Magnesium Oxide Nanoparticles. *Front. Bioeng. Biotechnol.* **2022**. [CrossRef]
24. Fouda, A.; Hassan, S.E.-D.; Saied, E.; Hamza, M.F. Photocatalytic degradation of real textile and tannery effluent using biosynthesized magnesium oxide nanoparticles (MgO-NPs), heavy metal adsorption, phytotoxicity, and antimicrobial activity. *J. Environ. Chem. Eng.* **2021**, *9*, 105346. [CrossRef]
25. Soliman, A.M.; Abdel-Latif, W.; Shehata, I.H.; Fouda, A.; Abdo, A.M.; Ahmed, Y.M. Green Approach to Overcome the Resistance Pattern of *Candida* spp. Using Biosynthesized Silver Nanoparticles Fabricated by Penicillium chrysogenum F9. *Biol. Trace Elem. Res.* **2021**, *199*, 800–811. [CrossRef] [PubMed]
26. Fouda, A.; Abdel-Maksoud, G.; Abdel-Rahman, M.A.; Eid, A.M.; Barghoth, M.G.; El-Sadany, M.A.-H. Monitoring the effect of biosynthesized nanoparticles against biodeterioration of cellulose-based materials by Aspergillus niger. *Cellulose* **2019**, *26*, 6583–6597. [CrossRef]
27. Hamza, M.F.; Abdel-Rahman, A.A.H.; Guibal, E. Magnetic glutamine-grafted polymer for the sorption of U(VI), Nd(III) and Dy(III). *J. Chem. Technol. Biotechnol.* **2018**, *93*, 1790–1806. [CrossRef]
28. Hamza, M.F.; Ahmed, F.Y.; El-Aassy, I.; Fouda, A.; Guibal, E. Groundwater purification in a polymetallic mining area (SW Sinai, Egypt) using functionalized magnetic chitosan particles. *Water Air Soil Pollut.* **2018**, *229*, 360. [CrossRef]
29. Alsharif, S.M.; Salem, S.S.; Abdel-Rahman, M.A.; Fouda, A.; Eid, A.M.; Hassan, S.E.-D.; Awad, M.A.; Mohamed, A.A. Multifunctional properties of spherical silver nanoparticles fabricated by different microbial taxa. *Heliyon* **2020**, *6*, e03943. [CrossRef] [PubMed]
30. Badawy, A.A.; Abdelfattah, N.A.H.; Salem, S.S.; Awad, M.F.; Fouda, A. Efficacy Assessment of Biosynthesized Copper Oxide Nanoparticles (CuO-NPs) on Stored Grain Insects and Their Impacts on Morphological and Physiological Traits of Wheat (*Triticum aestivum* L.) Plant. *Biology* **2021**, *10*, 233. [CrossRef]
31. Lashin, I.; Fouda, A.; Gobouri, A.A.; Azab, E.; Mohammedsaleh, Z.M.; Makharita, R.R. Antimicrobial and In Vitro Cytotoxic Efficacy of Biogenic Silver Nanoparticles (Ag-NPs) Fabricated by Callus Extract of *Solanum incanum* L. *Biomolecules* **2021**, *11*, 341. [CrossRef] [PubMed]
32. Kabay, N.; Solak, O.; Arda, M.; Topal, U.; Yuksel, M.; Trochimczuk, A.; Streat, M. Packed column study of the sorption of hexavalent chromium by novel solvent impregnated resins containing aliquat 336: Effect of chloride and sulfate ions. *React. Funct. Polym.* **2005**, *64*, 75–82. [CrossRef]
33. El-Hussaini, O.M.; Lasheen, T.A.; Helmy, E.M.; Hady, M.A.; Manaa, A.-S.A. Liquid-liiquid extraction/recovery of chromium(VI) from some industrial waste solutions using Alamine 336 in kerosene. *J. Dispers. Sci. Technol.* **2012**, *33*, 1179–1187. [CrossRef]
34. Morales, D.V.; Kusku, O.; Rivas, B.L.; Arda, M.; Kabay, N.; Bryjak, M. Removal of Cr(VI) by stabilized solvent impregnated resin (SIR) prepared by using a hydrophilic polymer adsorbent and Aliquat 336. *J. Chil. Chem. Soc.* **2019**, *64*, 4432–4436. [CrossRef]
35. Hamza, M.F.; El-Aassy, I.E.; Guibal, E. Integrated treatment of tailing material for the selective recovery of uranium, rare earth elements and heavy metals. *Miner. Eng.* **2019**, *133*, 138–148. [CrossRef]
36. Hamza, M.F.; Roux, J.-C.; Guibal, E. Metal valorization from the waste produced in the manufacturing of Co/Mo catalysts: Leaching and selective precipitation. *J. Mater. Cycles Waste Manag.* **2019**, *21*, 525–538. [CrossRef]
37. Hamza, M.F. Grafting of quaternary ammonium groups for uranium (VI) recovery: Application on natural acidic leaching liquor. *J. Radioanal. Nucl. Chem.* **2019**, *322*, 519–532. [CrossRef]
38. Yao, F.; Jia, M.; Yang, Q.; Luo, K.; Chen, F.; Zhong, Y.; He, L.; Pi, Z.; Hou, K.; Wang, D.; et al. Electrochemical Cr(VI) removal from aqueous media using titanium as anode: Simultaneous indirect electrochemical reduction of Cr(VI) and in-situ precipitation of Cr(III). *Chemosphere* **2020**, *260*, 127537. [CrossRef]

39. Hamza, M.F.; Wei, Y.; Mira, H.; Adel, A.-H.; Guibal, E. Synthesis and adsorption characteristics of grafted hydrazinyl amine magnetite-chitosan for Ni(II) and Pb(II) recovery. *Chem. Eng. J.* **2019**, *362*, 310–324. [CrossRef]
40. Javadian, H.; Ruiz, M.; Saleh, T.A.; Sastre, A.M. Ca-alginate/carboxymethyl chitosan/$Ni_{0.2}Zn_{0.2}Fe_{2.6}O_4$ magnetic bionanocomposite: Synthesis, characterization and application for single adsorption of $Nd^{+3}$, $Tb^{+3}$, and $Dy^{+3}$ rare earth elements from aqueous media. *J. Mol. Liq.* **2020**, *306*, 112760. [CrossRef]
41. Javadian, H.; Ruiz, M.; Taghavi, M.; Sastre, A.M. Synthesis of magnetic CMC bionanocomposite containing a novel biodegradable nanoporous polyamide selectively synthesized in ionic liquid as green media: Investigation on $Nd^{+3}$, $Tb^{+3}$, and $Dy^{+3}$ rare earth elements adsorption. *J. Mol. Liq.* **2020**, *308*, 113017. [CrossRef]
42. Stopa, L.C.B.; Yamaura, M. Uranium removal by chitosan impregnated with magnetite nanoparticles: Adsorption and desorption. *Int. J. Nucl. Energy Sci. Technol.* **2010**, *5*, 283–289. [CrossRef]
43. Tran, H.V.; Tran, L.D.; Nguyen, T.N. Preparation of chitosan/magnetite composite beads and their application for removal of Pb(II) and Ni(II) from aqueous solution. *Mater. Sci. Eng. C* **2010**, *30*, 304–310. [CrossRef] [PubMed]
44. Morales, M.A.; de Souza Rodrigues, E.C.; de Amorim, A.S.C.M.; Soares, J.M.; Galembeck, F. Size selected synthesis of magnetite nanoparticles in chitosan matrix. *Appl. Surf. Sci.* **2013**, *275*, 71–74. [CrossRef]
45. Elwakeel, K.Z.; Al-Bogami, A.S.; Elgarahy, A.M. Efficient retention of chromate from industrial wastewater onto a green magnetic polymer based on shrimp peels. *J. Polym. Environ.* **2018**, *26*, 2018–2029. [CrossRef]
46. Freire, T.M.; Fechine, L.M.U.D.; Queiroz, D.C.; Freire, R.M.; Denardin, J.C.; Ricardo, N.M.P.S.; Rodrigues, T.N.B.; Gondim, D.R.; Junior, I.J.S.; Fechine, P.B.A. Magnetic porous controlled $Fe_3O_4$-chitosan nanostructure: An ecofriendly adsorbent for efficient removal of azo dyes. *Nanomaterials* **2020**, *10*, 1194. [CrossRef] [PubMed]
47. Valverde Duran, S.; Lapo, B.; Meneses, M.; Maria Sastre, A. Recovery of neodymium (III) from aqueous phase by chitosan-manganese-ferrite magnetic beads. *Nanomaterials* **2020**, *10*, 1204. [CrossRef] [PubMed]
48. Dhivya, S.M.; Sathiya, S.M.; Manivannan, G.; Rajan, M.A.J. A comparative study on the biopolymer functionalized iron oxide nanocomposite for antimicrobial activity. *Mater. Today-Proc.* **2016**, *3*, 3866–3871. [CrossRef]
49. Hamza, M.F.; Fouda, A.; Wei, Y.; El Aassy, I.E.; Alotaibi, S.H.; Guibal, E.; Mashaal, N.M. Functionalized biobased composite for metal decontamination–Insight on uranium and application to water samples collected from wells in mining areas (Sinai, Egypt). *Chem. Eng. J.* **2022**, *431*, 133967. [CrossRef]
50. Hamza, M.F.; Fouda, A.; Elwakeel, K.Z.; Wei, Y.; Guibal, E.; Hamad, N.A. Phosphorylation of guar gum/magnetite/chitosan nanocomposites for uranium (VI) sorption and antibacterial applications. *Molecules* **2021**, *26*, 1920. [CrossRef]
51. Fouda, A.; Salem, S.S.; Wassel, A.R.; Hamza, M.F.; Shaheen, T.I. Optimization of green biosynthesized visible light active CuO/ZnO nano-photocatalysts for the degradation of organic methylene blue dye. *Heliyon* **2020**, *6*, e04896. [CrossRef] [PubMed]
52. Ruiz, M.; Sastre, A.; Guibal, E. Pd and Pt recovery using chitosan gel beads. I. influence of the drying process on diffusion properties. *Sep. Sci. Technol.* **2002**, *37*, 2143–2166. [CrossRef]
53. Djelad, A.; Morsli, A.; Robitzer, M.; Bengueddach, A.; di Renzo, F.; Quignard, F. Sorption of Cu(II) ions on chitosan-zeolite X composites: Impact of gelling and drying conditions. *Molecules* **2016**, *21*, 109. [CrossRef] [PubMed]
54. Zohuriaan, M.J.; Shokrolahi, F. Thermal studies on natural and modified gums. *Polym. Test.* **2004**, *23*, 575–579. [CrossRef]
55. Gad, Y.H. Preparation and characterization of poly(2-acrylamido-2-methylpropane-sulfonic acid)/Chitosan hydrogel using gamma irradiation and its application in wastewater treatment. *Radiat. Phys. Chem.* **2008**, *77*, 1101–1107. [CrossRef]
56. Duarte, M.L.; Ferreira, M.C.; Marvao, M.R.; Rocha, J. An optimised method to determine the degree of acetylation of chitin and chitosan by FTIR spectroscopy. *Int. J. Biol. Macromol.* **2002**, *31*, 1–8. [CrossRef]
57. Hamza, M.F.; Abdel-Rahman, A.A.-H. Extraction studies of some hazardous metal ions using magnetic peptide resins. *J. Dispers. Sci. Technol.* **2015**, *36*, 411–422. [CrossRef]
58. Hamza, M.F.; Hamad, N.A.; Hamad, D.M.; Khalafalla, M.S.; Abdel-Rahman, A.A.-H.; Zeid, I.F.; Wei, Y.; Hessien, M.M.; Fouda, A.; Salem, W.M. Synthesis of Eco-Friendly Biopolymer, Alginate-Chitosan Composite to Adsorb the Heavy Metals, Cd(II) and Pb(II) from Contaminated Effluents. *Materials* **2021**, *14*, 2189. [CrossRef] [PubMed]
59. Hamza, M.F.; Salih, K.A.; Adel, A.-H.; Zayed, Y.E.; Wei, Y.; Liang, J.; Guibal, E. Sulfonic-functionalized algal/PEI beads for scandium, cerium and holmium sorption from aqueous solutions (synthetic and industrial samples). *Chem. Eng. J.* **2021**, *403*, 126399. [CrossRef]
60. Corazzari, I.; Nistico, R.; Turci, F.; Faga, M.G.; Franzoso, F.; Tabasso, S.; Magnacca, G. Advanced physico-chemical characterization of chitosan by means of TGA coupled on-line with FTIR and GCMS: Thermal degradation and water adsorption capacity. *Polym. Degrad. Stab.* **2015**, *112*, 1–9. [CrossRef]
61. Wei, Y.; Salih, K.A.; Lu, S.; Hamza, M.F.; Fujita, T.; Vincent, T.; Guibal, E. Amidoxime functionalization of algal/polyethyleneimine beads for the sorption of Sr (II) from aqueous solutions. *Molecules* **2019**, *24*, 3893. [CrossRef] [PubMed]
62. Wei, Y.; Salih, K.A.; Hamza, M.F.; Fujita, T.; Rodríguez-Castellón, E.; Guibal, E. Synthesis of a New Phosphonate-Based Sorbent and Characterization of Its Interactions with Lanthanum (III) and Terbium (III). *Polymers* **2021**, *13*, 1513. [CrossRef] [PubMed]
63. Coates, J. Interpretation of Infrared Spectra, A Practical Approach. In *Encyclopedia of Analytical Chemistry*; John Wiley & Sons Ltd.: Hoboken, NJ, USA, 2006; pp. 1–23.
64. Imran, M.; Sajwan, M.; Alsuwayt, B.; Asif, M. Synthesis, characterization and anticoagulant activity of chitosan derivatives. *Saudi Pharm. J.* **2020**, *28*, 25–32. [CrossRef] [PubMed]
65. Xiang, Y.; Yang, M.; Guo, Z.; Cui, Z. Alternatively chitosan sulfate blending membrane as methanol-blocking polymer electrolyte membrane for direct methanol fuel cell. *J. Membr. Sci.* **2009**, *337*, 318–323. [CrossRef]

66. Caetano, C.S.; Caiado, M.; Farinha, J.; Fonseca, I.M.; Ramos, A.M.; Vital, J.; Castanheiro, J.E. Esterification of free fatty acids over chitosan with sulfonic acid groups. *Chem. Eng. J.* **2013**, *230*, 567–572. [CrossRef]
67. Hamza, M.F.; Roux, J.-C.; Guibal, E. Uranium and europium sorption on amidoxime-functionalized magnetic chitosan microparticles. *Chem. Eng. J.* **2018**, *344*, 124–137. [CrossRef]
68. Simonin, J.-P. On the comparison of pseudo-first order and pseudo-second order rate laws in the modeling of adsorption kinetics. *Chem. Eng. J.* **2016**, *300*, 254–263. [CrossRef]
69. Persson, I. Hydrated metal ions in aqueous solution: How regular are their structures? *Pure Appl. Chem.* **2010**, *82*, 1901–1917. [CrossRef]
70. Yang, Y.J.; Alexandratos, S.D. Affinity of polymer-supported reagents for lanthanides as a function of donor atom polarizability. *Ind. Eng. Chem. Res.* **2009**, *48*, 6173–6187. [CrossRef]
71. Pearson, R.G. Acids and bases. *Science* **1966**, *151*, 172–177. [CrossRef] [PubMed]
72. Marcus, Y. *Ion Properties*; Marcel Dekker, Inc.: New York, NY, USA, 1997; p. 259.
73. Giraldo, J.D.; Rivas, B.L.; Elgueta, E.; Mancisidor, A. Metal ion sorption by chitosan-tripolyphosphate beads. *J. Appl. Polym. Sci.* **2017**, *134*, 45511. [CrossRef]
74. Yang, Z.; Huang, X.; Yao, X.; Ji, H. Thiourea modified hyper-crosslinked polystyrene resin for heavy metal ions removal from aqueous solutions. *J. Appl. Polym. Sci.* **2018**, *135*, 45568. [CrossRef]
75. Gomez-Serrano, V.; Macias-Garcia, A.; Espinosa-Mansilla, A.; Valenzuela-Calahorro, C. Adsorption of mercury, cadmium and lead from aqueous solution on heat-treated and sulphurized activated carbon. *Water Res.* **1998**, *32*, 1–4. [CrossRef]
76. Bayramoglu, G.; Tuzun, I.; Celik, G.; Yilmaz, M.; Arica, M.Y. Biosorption of mercury(II), cadmium(II) and lead(II) ions from aqueous system by microalgae *Chlamydomonas reinhardtii* immobilized in alginate beads. *Int. J. Miner. Process.* **2006**, *81*, 35–43. [CrossRef]
77. Mohan, D.; Kumar, H.; Sarswat, A.; Alexandre-Franco, M.; Pittman, C.U., Jr. Cadmium and lead remediation using magnetic oak wood and oak bark fast pyrolysis bio-chars. *Chem. Eng. J.* **2014**, *236*, 513–528. [CrossRef]
78. Ahmed, S.A. Removal of lead and sodium ions from aqueous media using natural wastes for desalination and water purification. *Desalin. Water Treat.* **2016**, *57*, 8911–8926. [CrossRef]
79. Bao, S.Y.; Li, K.; Ning, P.; Peng, J.H.; Jin, X.; Tang, L.H. Highly effective removal of mercury and lead ions from wastewater by mercaptoamine-functionalised silica-coated magnetic nano-adsorbents: Behaviours and mechanisms. *Appl. Surf. Sci.* **2017**, *393*, 457–466. [CrossRef]
80. Deniz, S.; Tasci, N.; Yetimoglu, E.K.; Kahraman, M.V. New thiamine functionalized silica microparticles as a sorbent for the removal of lead, mercury and cadmium ions from aqueous media. *J. Serb. Chem. Soc.* **2017**, *82*, 215–226. [CrossRef]
81. Tofan, L.; Paduraru, C.; Cretescu, I.; Ceica, A.; Neagu, V. Chelating sorbent containing two types of functional groups—Hydroxamic acid and amidoxime for lead(II) ions effluent management. *Environ. Eng. Manag. J.* **2010**, *9*, 113–118.
82. Othman, M.K.; Al-Qadri, F.A.; Al-Yusufy, F.A. Synthesis, physical studies and uptake behavior of: Copper(II) and lead(II) by Schiff base chelating resins. *Spectrochim. Acta Part A-Mol. Biomol. Spectrosc.* **2011**, *78*, 1342–1348. [CrossRef] [PubMed]
83. Abo-Farha, S.A.; Abdel-Aal, A.Y.; Ashour, I.A.; Garamon, S.E. Removal of some heavy metal cations by synthetic resin purolite C100. *J. Hazard. Mater.* **2009**, *169*, 190–194. [CrossRef] [PubMed]
84. Khalil, T.E.; El-Dissouky, A.; Rizk, S. Equilibrium and kinetic studies on $Pb^{2+}$, $Cd^{2+}$, $Cu^{2+}$ and $Ni^{2+}$ adsorption from aqueous solution by resin 2,2′-(ethylenedithio)diethanol immobilized Amberlite XAD-16 (EDTDE-AXAD-16) with chlorosulphonic acid. *J. Mol. Liq.* **2016**, *219*, 533–546. [CrossRef]
85. Arar, O. Removal of lead(II) from water by di(2-ethylhexyl) phosphate containing ion exchange resin. *Desalin. Water Treat.* **2014**, *52*, 3197–3205. [CrossRef]
86. Hayeeye, F.; Yu, Q.J.; Sattar, M.; Chinpa, W.; Sirichote, O. Adsorption of $Pb^{2+}$ ions from aqueous solutions by gelatin/activated carbon composite bead form. *Adsorpt. Sci. Technol.* **2018**, *36*, 355–371. [CrossRef]
87. Bhatt, R.R.; Shah, B.A. Sorption studies of heavy metal ions by salicylic acid-formaldehyde-catechol terpolymeric resin: Isotherm, kinetic and thermodynamics. *Arab. J. Chem.* **2015**, *8*, 414–426. [CrossRef]
88. Zhang, L.; Wang, Y.; Huang, J.; Yuan, S. Azido chelating fiber: Synthesis, characterization and adsorption performances towards $Hg^{2+}$ and $Pb^{2+}$ from water. *Polym. Adv. Technol.* **2017**, *28*, 1418–1427. [CrossRef]
89. Massart, R. Preparation of aqueous magnetic liquids in alkaline and acidic media. *IEEE Trans. Magn.* **1981**, *17*, 1247–1249. [CrossRef]
90. Lopez-Ramon, M.V.; Stoeckli, F.; Moreno-Castilla, C.; Carrasco-Marin, F. On the characterization of acidic and basic surface sites on carbons by various techniques. *Carbon* **1999**, *37*, 1215–1221. [CrossRef]
91. Davies, W.; Gray, W. A rapid and specific titrimetric method for the precise determination of uranium using iron(II) sulphate as reductant. *Talanta* **1964**, *11*, 1203–1211. [CrossRef]
92. Mathew, K.J.; Buerger, S.; Vogt, S.; Mason, P.; Morales-Arteaga, M.E.; Narayanan, U.I. Uranium assay determination using Davies and Gray titration: An overview and implementation of GUM for uncertainty evaluation. *J. Radioanal. Nucl. Chem.* **2009**, *282*, 939–944. [CrossRef]
93. Marczenko, Z.; Balcerzak, M. Chapter 39—Rare-earth elements. In *Analytical Spectroscopy Library*; Elsevier: Amsterdam, The Netherlands, 2000; Volume 10, pp. 341–349.
94. Crank, J. *The Mathematics of Diffusion*, 2nd ed.; Oxford University Press: Oxford, UK, 1975; p. 414.
95. Tien, C. *Adsorption Calculations and Modeling*; Butterworth-Heinemann: Newton, MA, USA, 1994; p. 243.
96. Ho, Y.S.; McKay, G. Pseudo-second order model for sorption processes. *Process. Biochem.* **1999**, *34*, 451–465. [CrossRef]

97. Lima, É.C.; Dehghani, M.H.; Guleria, A.; Sher, F.; Karri, R.R.; Dotto, G.L.; Tran, H.N. CHAPTER 3—Adsorption: Fundamental aspects and applications of adsorption for effluent treatment. In *Green Technologies for the Defluoridation of Water*; Hadi Dehghani, M., Karri, R., Lima, E., Eds.; Elsevier: Amsterdam, The Netherlands, 2021; pp. 41–88.
98. Buema, G.; Lupu, N.; Chiriac, H.; Ciobanu, G.; Bucur, R.D.; Bucur, D.; Favier, L.; Harja, M. Performance assessment of five adsorbents based on fly ash for removal of cadmium ions. *J. Mol. Liq.* **2021**, *333*, 115932. [CrossRef]
99. Falyouna, O.; Eljamal, O.; Maamoun, I.; Tahara, A.; Sugihara, Y. Magnetic zeolite synthesis for efficient removal of cesium in a lab-scale continuous treatment system. *J. Colloid Interface Sci.* **2020**, *571*, 66–79. [CrossRef]